DOI:10.14753/SE.2020.2264

THEORETICAL METHODS FOR EXPLORING THE NEUROPHYSIOLOGICAL BEHAVIOR OF SINGLE NEURONS BASED ON EXPERIMENTAL DATA

PhD thesis

Dorottya Rita Cserpán

János Szentágothai Doctoral School of Neurosciences

Semmelweis University

Supervisor: Zoltán Somogyvári , Ph.D

Official reviewers: Richárd Fiáth , Ph.D
Lajos Kozák, MD, Ph.D

Head of the Complex Exam Committee: Alán Alpár, MD, D.Sc.

Members of the Complex Exam Committee: Árpád Dobolyi, D.Sc.
Emília Madarász, D.Sc.

Budapest
2018

DOI:10.14753/SE.2020.2264

Contents

DOI:10.14753/SE.2020.2264

DOI:10.14753/SE.2020.2264

List of Abbreviations

CSD	**C**urrent **S**ource **D**ensity
EC	**E**xtra**Cellular** Potential
kCSD	**k**ernel **C**urrent **S**ource **D**ensity
LFP	**L**ocal **F**ield **P**otential
MEA	**M**ulti **E**lectrode **A**rray
MUA	**M**ulti **U**nit **A**ctivity
sCSD	**s**pike **C**urrent **S**ource **D**ensity
skCSD	**s**ingle **k**ernel **C**urrent **S**ource **D**ensity
SUA	**S**ingle **U**nit **A**ctivity

DOI:10.14753/SE.2020.2264

1 Introduction

1.1 Motivation for studying single neurons with multi-electrode arrays

We all observe, consider options, plan, predict and act during everyday tasks, such as, reaching the food, finding a potential sex partner and escape danger. This behavior is not unique to humans, majority of the animal kingdom possesses the organ required for these actions, the brain. Generally, more complex structure and bigger brain results in more advanced and refined versions of the behavior. Humans are capable of much more, they can overcome our physical limitations. They use tools to extend our memories, to move bigger distances, to conquer the originally unfriendly places of the earth. Furthermore, humans, like myself, want to understand how they function and why they are able to do these things.

1.1.1 Levels of functioning

The nervous system comes in various shapes, structure and complexity, hence the neurons are considered as basic functional building blocks. While a roundworm (Caenorhabditis elegans) is able to operate with 302 neurons, brown rats with around $2 \cdot 10^8$, humans have 10^{10} neurons. All these creatures have the same goal: to live and to produce offspring; and all of these and many other species are successful in it. The difference is in the complexity of these actions, which require more complex brains. Based on anatomy and functionality a human brain can be divided on high level to cerebrum, brainstem and cerebellum. As the next step, the cerebral cortex can be further split to lobes and then to areas, columns, minicolumns, microcolumns until the cell level is reached. In the quest for understanding ourselves, especially our cognitive functions, we can seek answers in multiple levels. The answers given by a philosopher, psychologist, neurobiologist and computational neuroscientist etc. will be different and complementary. Various questions and the state of the art of technology imply various tools to be used for the investigation.

1.1.2 Open questions on the level of single neuron

The time has come, when technical tools bring us closer to monitor the activity of single neurons and identify correlations with cognitive functions. As to mention few examples, the mirror cells [Rizzolatti et al. 2004] are active, not only when the subject is performing an action, but also if he sees it. A grandmother cell [Gross 2002] or Halle Berry concept

neuron [Quiroga et al. 2005] would fire by various sensory inputs, which are related to her. The world famous place [O'Keefe et al. 1971], head direction cell [Taube et al. 1990], grid [Hafting et al. 2005] and boundary cells [O'Keefe et al. 1996] help in creating a cognitive map. The newest is the bravery cell [Mikulovic et al. 2018], which increase the risk-taking behavior. Neurons are part of a network, and in many cases cannot be connected to be "responsible" for identifying concepts.

Even though the physical modeling models of neurons are advanced, it doesn't mean, that we know how a neuron processes the incoming signals and reacts to those. Based on the properties of the dendrites, soma, even conclusions regarding the non-linearity of computations [Wei et al. 2001] can be drawn. The most interesting would be to see, that in case of certain inputs, how does the cell react, that is to understand the computations related to cognitive functions.

1.1.3 Multielectrode arrays

Although, electophysiological studies started with Luigi Galvani in the 1780-ies, it was not until the 1870-ies that Richard Caton observed electrical signals from the surfaces of animal brains. The first human EEG (electroencephalography) was recorded by Hans Berger in the early 20th century and identified various waves. In these studies the recorded signals originated from a bunch of neurons, hence are related to the population activity of the brain. Meanwhile Camillo Golgi developed a method for staining neurons and Ramón y Cajal found proof to the neuron theory stating, that the functional and structural units of the brain are the neurons. The characteristic electrophysiological behavior of a neuron namely the action potential, was first measured by Alan Lloyd Hodgkin and Andrew Fielding Huxley by a micro-electrode from the axon of a giant squid.

Since then, a variety of methods are used to investigate the electrophysiological properties of neurons. To date, patch-clamp [Neher et al. 1976] is the most commonly used technique to monitor neuronal membrane potential. Despite its unquestionable utility it remains challenging to monitor the activity of a cell at more than one or two sites. Extracellular recordings, on the other hand, deliver a more global picture of neural activity [Buzsáki et al. 2012; Einevoll et al. 2013]. With modern multielectrodes and microelectrode arrays it is now possible to record neuronal activity from many thousands of channels [Buzsáki 2004; Berdondini et al. 2005; Obien et al. 2015]. However, this technique does not permit direct recording of membrane potentials but instead spiking activity [which may be of individual cells (single-unit activity, SUA) or multiple cells (multiunit activity or MUA, which is the mean firing rate of cell populations)] and components of postsynaptic activity visible at low frequencies (<300 Hz, so-called local field potential, LFP); see [Buzsáki et al. 2012; Einevoll et al. 2013; Głabska et al. 2016a] for discussion.

So far, the main advantages of high density array recordings have been improved resolution of spike detection [Rey et al. 2015], as more cells can be identified in a single recording, improved stimulation precision [Hottowy et al. 2012; Chichilnisky 2001], of particular importance for retinal neuroprosthetics, and new features observed in the profiles of slow fields [Ferrea et al. 2012]. Recently, high density probes have also been used in studies of axon tracking [Bakkum et al. 2013; Lewandowska et al. 2016] and multisynaptic integration [Jäckel et al. 2017].

Multielectrode recordings have been traditionally used for improved spike sorting [Buzsáki 2004; Berdondini et al. 2005; Obien et al. 2015; Muthmann et al. 2015] and for the reconstruction of current source densities (CSD) behind the recorded LFP [Pitts 1952; Mitzdorf 1985; "Current Source Density (CSD) Analysis"], although more specific methods have since been devised ["Local field potential: Biophysical origin and analysis"; Głabska et al. 2014; Głabska et al. 2016b]. Several attempts have been made, using different approaches, to localize cells from multielectrode recordings. For example, accounting for the properties of electric field propagation in the tissue [Muthmann et al. 2015], that form the basis of CSD methods [Somogyvári et al. 2005; Somogyvári et al. 2012], or other triangulation approaches [Mechler et al. 2011b; Mechler et al. 2011a]. We are not aware of any prior attempts, however, to reconstruct the CSD of individual neurons using their available morphologies, which we propose here.

Our method assumes we have a set of extracellular recordings, coming from a specific neuron, whose morphology and location with respect to the electrode is known, collected with multiple contacts. This could be realized experimentally by patching a neuron close to the multielectrode and driving it through an intracellular injection or monitoring its activity. In this way it is possible to determine the contribution of this specific cell to the extracellular field. Computing spike-triggered average of the potential, which we do in our proof-of-concept experiment, or driving the neuron with sinusoidal current and averaging the extracellular potential (EC) over periods of the driving current, are ways in which this could be achieved. When the recordings are complete, we inject dye into the cell and reconstruct its morphology. Thus we obtain a set of synchronous multichannel extracellular recordings reflecting the activity of a single neuron whose morphology is also known, as well as the position of the neuron relative to the electrode contacts. Here we show how to use this approach to infer the distribution of current sources based on cell morphology as they change in time. The data necessary to apply presented method have been available for some time [Henze et al. 2000; Gold et al. 2006], although recently have became much more comprehensive [Jäckel et al. 2017]. While we believe the estimation of transmembrane currents along the cell morphology using this type of data has not been reported previously, similar questions have been posed by [Gold et al. 2006], who attempted to identify the

biophysical properties of a neuron membrane based on the extracellular signature of the action potential. A similar strategy was used by [Frey et al. 2009] in their studies of extracellular action potential shape observed with high-definition multi-electrode arrays.

The *single cell kernel Current Source Density* method (skCSD) we introduce here is an application of the framework of the *kernel Current Source Density method* [Potworowski et al. 2012 to the data coming from a single cell. This is done by restricting current sources to cell morphology. This can be done efficiently for arbitrarily complex morphologies and arbitrary electrode configurations.

The importance of this work is that for the first time we show here how a collection of extracellular recordings in combination with cell morphology can be used to estimate how the current sources located on a studied cell contribute to the recorded field potential. Since it is feasible to acquire the relevant data, we believe that the method proposed here may be used to constrain the biophysical properties of the neuron membrane and facilitate consistency of the reconstructed morphology. Further, this method can help guide new discoveries by providing a more global picture of the current distribution based on neuronal morphology, leading to a coherent spatiotemporal view of synaptic drive and return currents of the observed neuron.

1.2 Monopole phenomena

There is ongoing discussion in the neuroscience society about the existence of current source monopoles. Riera et al. [Riera et al. 2012] measured the above mentioned phenomenon and several explanation appeared in various papers, though a satisfactory one still has not been provided. The central question is, that the long standing belief of instantaneous balance of neural currents, often referred as quasistatic approximation, fails or holds. The significance of this question extends well beyond itself, as Gratiy et al. [Gratiy et al. 2013] pointed out, since many electrophysiological theory from the Hodgkin-Huxley model to the interpretation of electrocardiograms use this basic assumption. Gratiy et al. raised two possible explanations, which could cause an observed monopole moment: First, that the currents carried by long neural processes leaving the observed volume of the electrode array could lead significant charge out, thus those currents will be missing from the CSD distribution, appearing as an unbalanced, monopole source. The second possibility according to them is, that the actually observed CSD distribution may not satisfy all the assumptions of the applied CSD calculation method, especially assumptions on the lateral distribution of the CSD far from the electrode. In a response Riera and Cabo [Riera et al. 2013], that the applied vCSD method [Cabo et al. 2014] uses 3D potential measurements and no assumptions on the lateral distribution of the CSD. Furthermore, that

DOI:10.14753/SE.2020.2264

the diameter of the dendritic tree of the observed cortical neuron types are well bellow the lateral extent of the applied electrode system, so this can not be the case. The pitfalls of the lateral assumptions could explain the earlier observation of unbalanced currents based on measurements of 1D electrode system [Somogyvári et al. 2005], but not the case described in [Riera et al. 2012].

DOI:10.14753/SE.2020.2264

2 Objectives

2.1 Monopole current sources explained

As there is the ongoing discussion about the emergence of the monopole source, which contradicts the quasistatic estimation of charge conservation, we aim to understand and explain the possible causes leading to this observation. We state, that the finite spatial sampling of the extracellular medium strongly contributes to the emergence of monopole current sources. Therefore, we simulate the electrophysiological behavior of a neuron and calculate the extracellular potential at certain points in space. These points are chosen to form a grid of various inter-electrode distances. The traditional CSD and the vCSD methods are used to estimate the current source density distribution. The monopole, dipole and quadrupole moments are calculated and compared.

2.2 Sensitivity of sCSD method to the arrangement

One of the key assumptions of the sCSD method is, that the main axis of the cell is parallel to the electrode. Although, this is roughly possible experimentally, for example when recording from pyramidal neurons the linear probe is inserted perpendicular to the brain surface. Therefore, we wanted to investigate, how much distortion in the result is done when our assumption is not met. As shown in 2.1, we described the position of the cell with the (d) distance of the soma from the electrode and with 2 angles, α marks the angle between being parallel and the main axis of the cell, β shows the rotation around the x axis. To see the effect, we created known current source distributions and a certain α, β and d and performed the reconstruction as if the cell was perfectly parallel with the linear probe.

2.3 Development of the skCSD method

The skCSD method aims to provide information about the fine details of the electrophysiological behavior of an observed cell by estimating the membrane current source density distributions. Due to the high temporal and spatial resolution of the multielectrodes used for recording and hence providing the extracellular potentials to the skCSD method, the resolution of the method is below ms and few tens of μm. Definitely such a new method must stand must be tested in diverse situations. This goal is challenging in terms of experimental and theoretical methods as well, but the first one we leave to others. As the

DOI:10.14753/SE.2020.2264

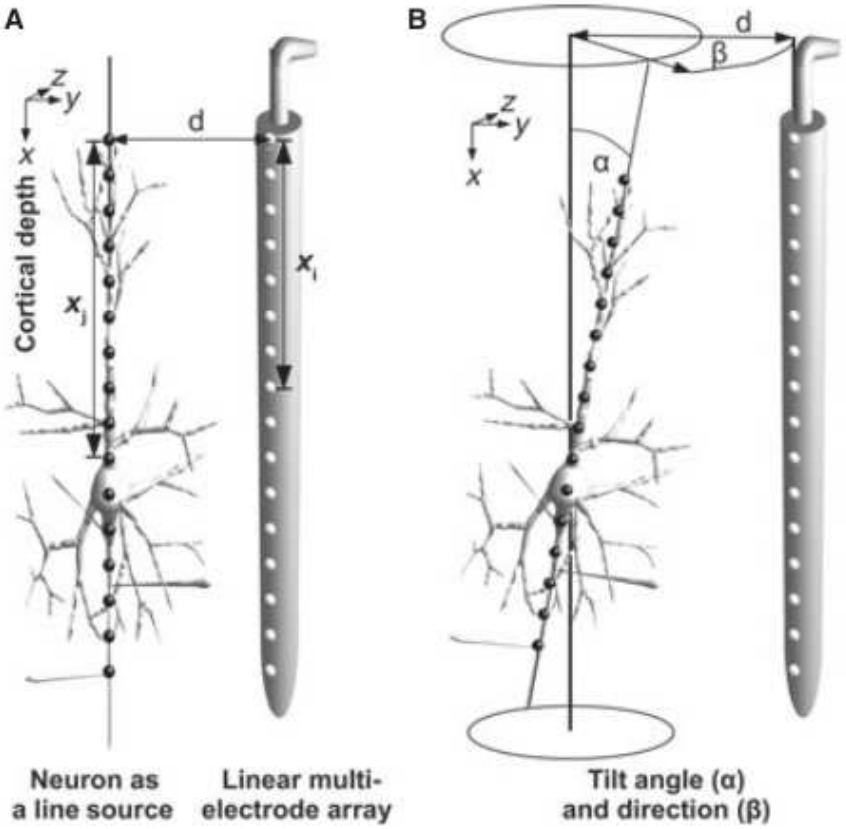

Figure 2.1: ***Schematic figure about the ideal experimental setup and when the cell is tilted and rotated.*** *In the ideal case, the main axis of the cell is parallel and each current sources marked by grey dots are d distance away from the electrodes. When the cell is tilted with* α *and rotated with* β*, d marks the distance of the soma from the nearest electrode.*

basis of the mathematical model we rely on the already existing current source density method and build on these our novel ideas and approaches.

The first milestone was to create the theoretical relationship between the continuous membrane CSD distribution and the finite sampled extracellular potentials. Second, validation of the method is vital, for this reason simulated data was generated. In this way the ground truth is known and we could construct various scenarios from simple to complex ones. As a third milestone, we applied the method on real experimental data.

DOI:10.14753/SE.2020.2264

3 Methods

The content of this chapter is a guide and description of the method, the techniques and the experimental data used in the following chapter.

3.1 Overview of current source density reconstruction methods

The methods described here are all used with the exception of the inverse CSD for deriving our results, which was included here for the completeness of the list.

3.1.1 Traditional CSD

For the reader's convenience, here we briefly present the basic ideas behind the traditional and recent approaches to reconstruction of current source density (CSD analysis).

The relation between current sources in the tissue and the recorded potentials is given by the Poisson equation

$$C = -\nabla(\sigma \nabla V), \tag{3.1}$$

where C stands for CSD and V for the potential. While this can be studied numerically for nontrivial conductivity profiles [Torbjrn et al. 2016], here we shall mostly assume a constant and homogeneous conductivity tensor, σ. In that case, the above equation simplifies to $C = -\sigma \Delta V$ and can be solved for C given the potential in the whole space. On the other hand, given the potential in the whole space, the potential is given by

$$V(\mathbf{x}) = \frac{1}{4\pi\sigma} \int d^3\mathbf{x}' \, \frac{C(\mathbf{x}')}{|\mathbf{x} - \mathbf{x}'|}. \tag{3.2}$$

The *traditional CSD method* relies on the discretised, 1 dimensional (z) form of the Poisson-equation

$$C(z) = -\sigma \frac{d^2 V(z)}{dz^2} \tag{3.3}$$

Walter Pitts observed that having recordings on a regular grid of electrodes we can estimate CSD by taking numerical second derivative of the potential [Pitts 1952], we call this approach *traditional CSD method*. Pitt's idea gained popularity only after Nicholson and Freeman popularized its use for laminar recordings [Nicholson et al. 1975] in the cortex. Considering the assumptions below:

- quasistatic approximation of Maxwell's equations
- linear extracellular medium
- ohmic (resistive) medium

the following approximation can be derived:

$$C(z_j) = -\sigma \frac{V(z_j+h) - 2V(z_j) + V(z_j-h)}{h^2}, \tag{3.4}$$

where z_j is the position of the j^{th} electrode and h is the inter-electrode distance. As this is based on the finite differences solution and the precision is of order $O(h^2)$, in higher dimension the error of the approximation is even bigger. Furthermore, the CSD method relies on several other

3.1.2 Inverse CSD (iCSD)

To overcome limitations of the traditional approach, such as difficulty of handling the data at the boundary and hidden assumptions about the dimensions we do not probe, Pettersen et al. proposed a model-based *inverse CSD method* [Pettersen et al. 2006]. Initially proposed in 1D, the method was later generalized to other dimensionalities [Łeski et al. 2007; Łeski et al. 2011]. Given a set of recordings $V_1, \ldots, V_N$ at regularly placed electrodes at $\mathbf{x}_1, \ldots, \mathbf{x}_N$ this method assumes a model of CSD parameterized with CSD values at the measurement points, $C(\mathbf{x}) = \sum_{k=1}^{N} C_k f_k(\mathbf{x})$, where $f_k(\mathbf{x})$ are functions taking 1 at $\mathbf{x}_k$, 0 at other measurement points, with the values at other points defined by the specific variant of the method, for example, spline interpolated in spline iCSD ["Current Source Density (CSD) Analysis"]. Assuming the model $C(\mathbf{x})$ one computes the potential at the electrode positions obtaining a relation between the model parameters, C_k, and the measured potential, V_k, which can be inverted leading to an estimate of the CSD in the region of interest.

3.1.3 Volume CSD (vCSD)

The method Riera et al. 2014 estimates the currents as point sources distributed evenly along a 3-dimensional grid. The current distribution (C) is calculated from the extracellular potential (V) by the following formula:

$$C = (G'G + \lambda L'L)^{-1} G'V \tag{3.5}$$

where G is the discrete generalized Green's function matrix, L is the discrete spatial Laplacian operator, λ is the regularization parameter. In this case, the ij-th element of G takes the value of:

$$G_{ij} = \frac{1}{4\pi d_{ij}}, \tag{3.6}$$

where d_{ij} is the distance between the i-th electrode and j-th current source. According to our experience, this method may give a better reconstruction of the current source distribution compared to the traditional CSD method, but the result highly depends on the regularization parameter and the calculation is computationally very demanding. We used a regular grid with 50 μm interelectrode distance covering the whole volume of recording.

3.1.4 Kernel CSD (kCSD)

The kernel Current Source Density method [Potworowski et al. 2012] can be considered a generalization of the inverse CSD. It is a non-parametric method which allows reconstructions from arbitrarily placed electrodes and facilitates dealing with the noise. Conceptually, the method proceeds in two steps. First, one does kernel interpolation of the measured potentials. Next, one applies a "cross-kernel" to shift the interpolated potential from the potential to the CSD space. In 3D space, in a homogeneous and isotropic conductivity field, this amounts to applying the Laplacian to the interpolated potential, Eq. (3.1). To handle all cases in a general way, including data of lower dimensionality or with non-trivial conductivity, we construct the interpolating kernel and cross-kernel from a collection of basis functions. The idea is to consider current source density in the form of a linear combination of basis sources $\widetilde{b}_j(\mathbf{x})$, for example Gaussians,

$$C(\mathbf{x}) = \sum_{j=1}^{M} a_j \widetilde{b}_j(\mathbf{x}), \tag{3.7}$$

where the number of basis sources $M \gg N$, the number of electrodes, and a_j are the weights with which the basis sources are combined into the model CSD. Let $b_j(\mathbf{x})$ be the contribution to the extracellular potential from $\widetilde{b}_j(\mathbf{x})$, which in 3D is

$$b_j(x,y,z) = \mathscr{A}\widetilde{b}_j(x,y,z) = \frac{1}{4\pi\sigma}\int dx' \int dy' \int dz' \frac{\widetilde{b}_j(x',y',z')}{\sqrt{(x-x')^2+(y-y')^2+(z-z')^2}}, \tag{3.8}$$

but in 1D or 2D we would need to take into account the directions we do not control in the experiment (for example, along the slice thickness for a slice placed on a 2D MEA). There exists a linear operator $\mathscr{A}$: *space of sources*$\rightarrow$ *space of potentials*, that the potential will

have a form

$$V(\mathbf{x}) = \mathscr{A}C(\mathbf{x}) = \sum_{i=1}^{M} a_i b_i(\mathbf{x}). \tag{3.9}$$

Since we cannot estimate M coefficients a_j from N measurements for $N < M$, we construct a kernel for interpolation of the potential,

$$K(\mathbf{x},\mathbf{x}') = \sum_{i=1}^{M} b_i(\mathbf{x}) b_i(\mathbf{x}'). \tag{3.10}$$

Then, any potential field $V(\mathbf{x})$ spanned by $b_i(\mathbf{x})$ can be written as

$$V(\mathbf{x}) = \sum_{l=1}^{L} \beta_l K(\mathbf{x}_l,\mathbf{x}), \tag{3.11}$$

for some L, $\mathbf{x}_l$, and β_l, but it minimizes the regularized prediction error

$$\sum_{k=1}^{N} (V(\mathbf{x}_k) - V_k)^2 + \lambda \sum_{l=1}^{L} \beta_l^2, \tag{3.12}$$

when $L = N$. Here, $\mathbf{x}_k$ are the positions of the electrodes, V_k are the corresponding measurements, λ is the regularization constant. The minimizing solution is obtained for

$$\beta = (\mathbf{K} + \lambda \mathbf{I})^{-1} \cdot \mathbf{V}. \tag{3.13}$$

where $\mathbf{V}$ is the vector of the measurements V_k, and $\mathbf{K}_{jk} = K(\mathbf{x}_j,\mathbf{x}_k)$.

To estimate CSD we introduce a cross-kernel

$$\widetilde{K}(\mathbf{x},\mathbf{x}') = \sum_{j=1}^{M} b_j(\mathbf{x}) \widetilde{b}_j(\mathbf{x}'). \tag{3.14}$$

If we define

$$\widetilde{\mathbf{K}}^T(\mathbf{x}) := [\widetilde{K}(\mathbf{x}_1,\mathbf{x}),\ldots,\widetilde{K}(\mathbf{x}_N,\mathbf{x})],$$

then the estimated CSD takes form of

$$C^*(\mathbf{x}) = \widetilde{\mathbf{K}}^T(\mathbf{x}) \cdot (\mathbf{K} + \lambda \mathbf{I}))^{-1} \cdot \mathbf{V}, \tag{3.15}$$

where λ is the regularization parameter and $\mathbf{I}$ the identity matrix; see [Potworowski et al. 2012] for derivation and discussion.

3.1.5 Spike CSD (sCSD)

The Spike CSD [Somogyvári et al. 2012] is the forerunner of the method presented here, as it aims to estimate the current source distribution of single neurons with unknown morphology. The sCSD method provides an estimation of the cell-electrode distance and uses a simplified model of the shape of the neuron to reach this. Separating potential patterns generated by different neurons is critical and it is obtained by clustering extracellular fingerprints of action potentials which are different for every neuron. The limitation of sCSD is the assumed simplified morphology of the model and low spatial resolution. Despite that, even with this simplified model, it was possible to demonstrate for the first time the EC observability of backpropagating action potentials in the basal dendrites of cortical neurons, the forward propagation preceding the action potential on the dendritic tree and the signs of the Ranvier-nodes [Somogyvári et al. 2012].

Theoretical formalism In this approach, the current source density distribution of a cell will be modelled as N point sources along a line, which is parallel with the linear probe, which has N recording sites. In this case the connection between the recorded potentials and the point sources can be describes by the discrete form of the Poisson equation can be written as:

$$V_i(r_i) = \frac{1}{4\pi\sigma} \sum_{j=1}^{N} \frac{C_j}{|r_i - p_j|,} \tag{3.16}$$

where r_i is the position of the i-th electrode and p_j of the j-th current source. It can be written also in a matrix formalism:

$$\mathbf{V} = \mathbf{TC} \tag{3.17}$$

Where T is the transfer matrix. In order to get the current sources:

$$\mathbf{C} = \mathbf{T^{-1}V} \tag{3.18}$$

Where the elements of T can be calculated as

$$T_{ij} = \frac{1}{4\pi\sigma d_{ij}} \tag{3.19}$$

, where d_{ij} is the distance of the i-th electrode from the j-th current source. As d_{ij} is not known, a measure is introduced (Figure 3.1.C) based on apriori knowledge in order to get an estimation. This method focuses on estimating the CSD around the time of the spike, the expected CSD pattern can be used for creating a metric for estimating the correct distance. As at the emission of an action potential positive ions flow into and negative ions out from the soma, int the neighboring part of the cell membrane the opposite happens,

DOI:10.14753/SE.2020.2264

there is a balancing counter current. In cases of few tens of micrometers this should result in a sCSD pattern with a:

- peak at the level of the soma
- small, inverse signed values neighboring sources.

The following measure S captures this behavior:

$$S(d) = \frac{\sum I_{-s}(d) - |I_s|}{I_s(d)} \tag{3.20}$$

where d is the hypothetical cell to electrode distance for the reconstruction, I_s the reconstructed current source for the soma and $\sum I_{-s}$ is the sum of all the other current sources at the peak of the spike. The maximum value of this function will give the best assumption for the cell-to-electrode distance. Once the most appropriate distance is identified, it is straightforward to solve the Poisson equation for N point sources and N electrodes. The schematic description and main steps of the method are presented on Figure 3.1.

DOI:10.14753/SE.2020.2264

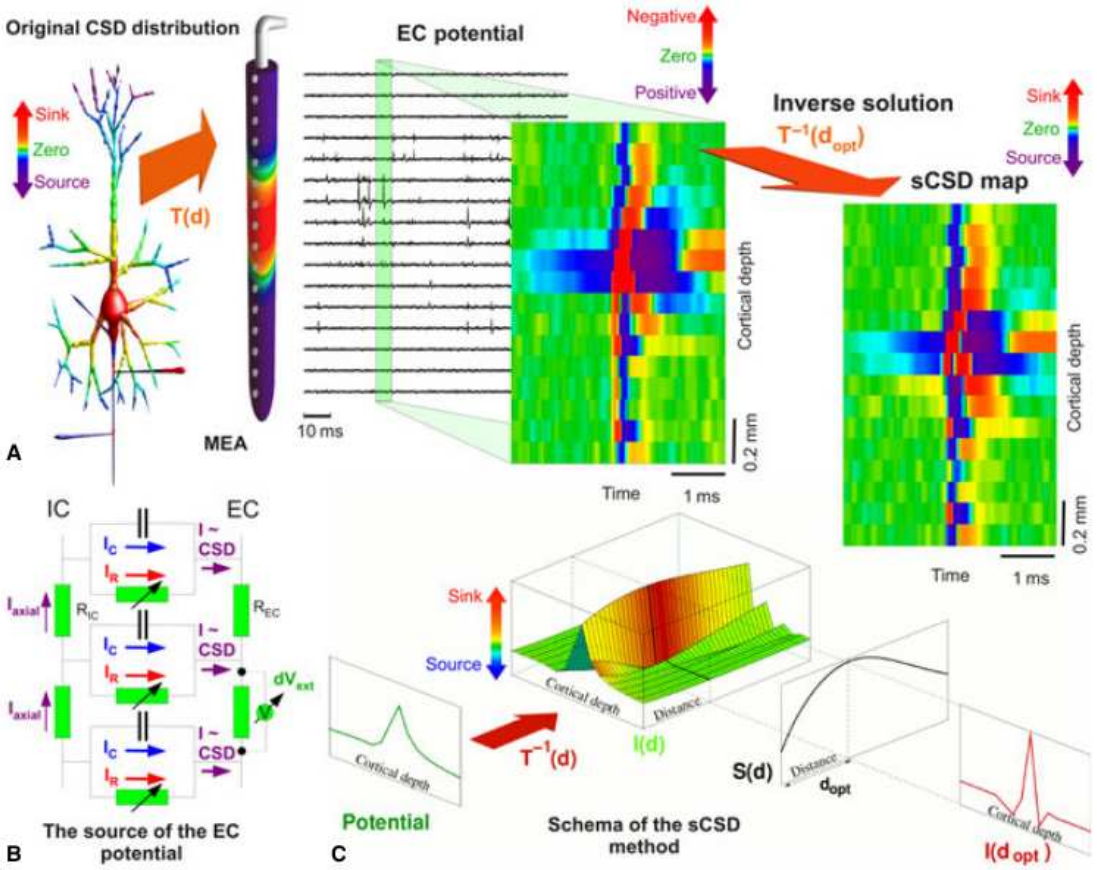

Figure 3.1: ***Schematic picture of the basic steps and assumptions of the sCSD method.*** *A. Assumed experimental setup. The linear probe is parallel to the main axis of the neuron. We model the current source distribution of the cell showed by the colorscale as N point current sources along the main axis of the cell. The exracellular potential is then recorded by N electrodes. On the measured extracellular potentials we take the potential with a certain time-window around a spike and on all channels, this is shown as spatio-temporal colormap of the extracellular potential. For a better signal-to-noise ratio we used the spike triggered averages. Then by using an estimated cell-to-electrode distance, the sCSD is calculated by using a transfer matrix. The resulting sCSD is also shown as a colormap, on which red color indicates current sinks, value colors current sources. B. Schematic figure shows the connection between currents and the extracellular potential. The CSD is composed of resistive and capacitive membrane currents and the extracellular potential at a point in space is the superposition of the potentials related to the CSD current sources. C. To get an estimation for the cell-to-electrode distance, a measure is introduced which finds the biologically most relevant distance based on the sCSD pattern at the spike. As the first step, the sCSD distributions are calculated for 1,2... 200 µm distances at the time of the spike. Then by using a measure, the peakiest spatial distribution is used, as by the time of the spike we expect a large current sink at the soma and small sources in the neighboring points.*

DOI:10.14753/SE.2020.2264

3.1.6 Technical tools for the validation of the CSD methods

3.1.6.1 Construction of ground truth data

To validate the method we used simulated data which allows us to consider arbitrary cell-electrode setups and test various current patterns. The LFPy package [Lindén et al. 2014] was used to simulate the extracellular potential at arbitrarily placed virtual electrodes. We assumed the `.swc` morphology description format Cannon et al. 1998 and the sections were further divided to segments. The coordinates of every segment's ends were used to find the connections. Once the connection matrix was calculated, we used the Chinese postman algorithm to obtain the morphology loop. We calculated the potential using neuron models with various morphologies shown in Fig. 3.2 and different input distributions, assuming one- and two-dimensional multielectrode arrays. We used toy models to better understand and characterize the method as well as a biologically realistic neuron model to estimate performance of skCSD in an experimentally realistic scenario.

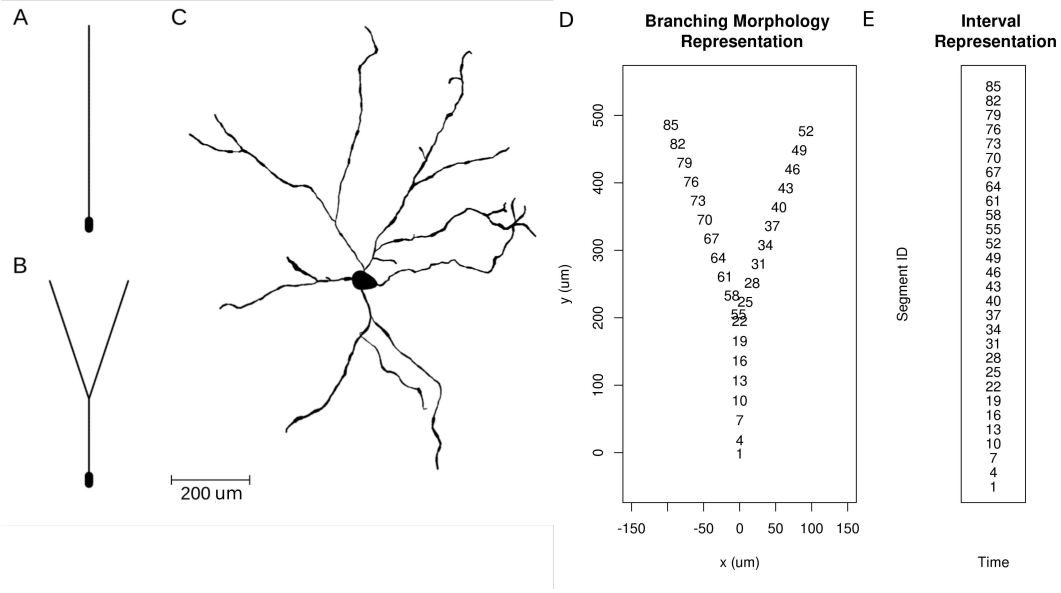

Figure 3.2: ***Neuron morphologies used for simulation of ground truth data.*** *A. Ball-and-stick neuron. B. Y-shaped neuron. C. Ganglion cell. D. Branching morphology representation of the Y-shaped neuron. The numbers show the segment ID of the morphology. E. Interval representation of the Y-shaped neuron. The dendrites of the neuron are aligned along a line.*

The simplest setup we used was a ball-and-stick neuron recorded with a laminar probe. Various artificial CSD patterns and also biologically more realistic CSD distributions served as test distributions in order to quantify the spatial resolution and reconstruction errors. To generate the ground truth data we simulated a 500 μm long linear cell model of 52 segments in LFPy. The diameter of the two segments representing the soma was 20 μm,

while the other segments were 4 μm wide. 100 synaptic excitation events were distributed randomly along this morphology in order to imitate a biologically realistic scenario.

To test the effect of branching on the results, a simple Y-shaped morphology was used (Fig. 3.2B). The synapses were placed at segments 33 and 62 on different branches close to the branching point. The first was stimulated at 5, 45, 60 ms, the other at 5, 25, 60 ms after the onset of the simulation. The idea here was to consider the inputs stimulated together and separately. The times of activation were randomly selected in such a way as to leave enough time for the membrane activity to settle down. This can be viewed as extreme cases of correlated and uncorrelated events. Note that the skCSD reconstruction is not affected directly by the temporal correlation of the synaptic inputs. Just like any CSD estimation method, skCSD is applied to the potentials recorded at a given point in time. Of course, it is affected indirectly, in the sense that slower or faster oscillating inputs lead to different spatial patterns due to filtering effects of the dendritic membrane: fast oscillations induce short dipoles, slow oscillations allow the current to spread along the cell leading to stronger dipoles [Lindén et al. 2010]. We address these effects indirectly in Fig. 4.10.

As a realistic example we used a mouse retinal ganglion cell morphology Kong et al. 2005 from NeuroMorpho.Org Ascoli 2006. In the simulations 608 segments were used. 100 synaptic excitation events were distributed randomly along this morphology within the first 400 ms of the simulation. The cell was also driven with an oscillatory current. In the dendrites, only passive ion channels were used.

Parameters of the simulations. We simulated three different model morphologies: ball-and-stick (BS), Y-shaped (Y), and a ganglion cell (Gang). The Y-shaped neuron was considered in two situations, when it was parallel (Y) or orthogonal (Y-rot) to the MEA plane. The extracellular potential was computed at multiple points modeling different experimentally viable recording configurations (cell and setup). All combinations used are summarized in Table 3.1. The parameters describing the neuron membrane physiology are given in Table 3.2. The length of the simulation was 70 s in case of the ball-and-stick and Y-shaped neurons, and 850 s for the ganglion cell model.

Parameters of synapses. In most simulations we modeled synaptic activity. We used synapses with discontinuous change in conductance at an event followed by an exponential decay with time constant τ (ExpSyn model as implemented in the NEURON simulator). When simulating the Y-shaped neuron we placed two synapses with the following parameters: reversal potential: 0 mV , synaptic time constant: 2 ms, synaptic weight: 0.04 μS. The synapses were placed at segments 33 and 62 (See Fig. 3.2 and 4.12). When simulating

Table 3.1: Main parameters of the simulated cells and setups.

	Cell Properties		**Synapse Properties**			**Distribution of Electrodes**	
	Length (μm)	Number of Seg.	Location (ID of Seg.)	Number of Syn.	Synaptic Weight (μS)	Type	Number
BS	516	53	random	100	0.01	linear	8,16, 32, 64, 128
Y	848	86	33, 62	6	0.04	rectangular, random	2x4, 4x4, 4x8, 4x16
Y-rot	848	86	33, 62	6	0.04	rectangular	8,16, 32, 64
Gang	5876	608	random	100	0.01	hexagonal, rectangular	128, 25, 49, 81, 441

Table 3.2: Biophysical parameters characterizing the simulated cell models.

Quantity	**Value**	**Unit**
Initial potential	-65	mV
Axial Resistance	123	Ωcm
Membrane resistivity	30000	Ωcm^2
Membrane capacitance	1	$\mu F/cm^2$
Passive mechanism reversal potential	-65	mV

the other models (ball-and-stick and ganglion cell) we used the same type of synapse, however, the synaptic weights were a quarter of the above (0.01 μS) since they were more numerous (Table 3.1).

3.1.6.2 Measuring the Quality of Reconstruction

To validate the skCSD method we need to consider two situations. When we know the ground truth — the actual distribution of sources which generated the measured potentials — we can compare the reconstruction with it. This is available directly only in simulations. In that case we can measure the prediction error between the reconstruction and the original. However, the skCSD method by its nature gives smooth results. This is a consequence of kernel interpolation of the potential which occurs in the first step of the method. The same phenomenon occurs in regular CSD estimation [“Current Source Density (CSD) Analysis”]. Thus, we can never recover the original CSD distribution but only a coarse-grained approximation. This is not a significant problem as the coarse-grained CSD should have equivalent physiological consequence. However, to compare the reconstructed density with the ground-truth, which is typically very irregular in consequence of multiple synaptic activation, we always smoothed the ground truth CSD with a Gaussian kernel. The width

of the kernel was 15 μm for ball-and-stick model, while for the Y-shaped and ganglion cell models we used 30 μm.

Thus, whenever ground truth was known, we computed L1 norm of the difference between the reconstruction C^* and smoothed ground truth C normalized by the L1 norm of C:

$$\varepsilon_{L1} = \frac{\sum_{segments,time} |\mathbf{C} - \mathbf{C}^*|}{\sum_{segments,time} |\mathbf{C}|}. \tag{3.21}$$

When analyzing experimental data we only have access to the noisy measurements and cannot apply the above strategy directly. Thus we consider two strategies. One is to use cross-validation error (CV). In leave-one-out cross-validation [Potworowski et al. 2012] we estimate CSD from all the measurements but one and compare estimated prediction with actual measurement on the removed electrode. Repeating this procedure for all the electrodes gives us a measure of prediction quality for a given set of parameters for this specific dataset. Scanning over some parameter range we identify optimal parameters as those giving minimum error. They are further used to analyze the complete data. The advantage of using cross-validation error is that it does not require the knowledge of the ground truth current source density distribution and can still provide an estimation about the performance of the skCSD method. As this algorithm is quadratic in the number of electrodes, for large arrays one might prefer to use the leave-p-out cross-validation instead. When we test how the quality of the reconstruction changes with the number of electrodes we use CV error normalized by the number of electrodes which can then be compared between different setups.

The other strategy we use and recommend in the experimental context. The idea is to simulate different current source distributions, either placing specific distribution by hand or by modeling activity of the cell assuming passive membrane and random or specific synaptic activation, both of which are relatively inexpensive both in computational time and coding complexity. This reduces the problem to the modeling case. We can use thus generated data (CSD and potentials) scanning for optimal reconstruction parameters to be used in analysis of actual experimental data from the setup.

To handle the effects of noise one should study its properties on electrodes, e.g., assuming white measurement noise identify its variance, then tune the regularization parameter λ on simulated sets with comparable simulated noise added.

3.1.6.3 Parameter selection

To apply the skCSD method we need to decide upon the number of basis functions, set their width (R), and choose the regularization parameter λ. In this work the number of

basis function was set to 512 for all cases, which is at least twice the number of electrodes used. This is usually not a limitation, the more the better. For the basis width (Eq. (4.5)) we took the following values: 8, 16, 32, 64, 128 μm. Selection of the regularization parameter is not trivial [Potworowski et al. 2012; *Discrete Inverse Problems*]. Here, we tested the effect of the regularization parameter taking values of 0.00001, 0.0001, 0.001, 0.01, 0.1 The optimal parameters were identified by the lowest value of reconstruction error.

3.1.6.4 Visual representation of CSD on the morphology

To visualize the distribution of current sources and other quantities along a neuron morphology we use two representations of the cell:

1. ***Interval representation***: we stack all the compartments consecutively along the y-axis so that the part of the dendrite stemming from the soma is shown first, followed by one branch, followed by the other. The order of the branches in the stack is taken from the morphology loop to make these representations consistent. The x-axis either shows different time instants of the simulations or various distribution patterns.

2. ***Branching morphology representation***: in this case a two-dimensional projection of the cell is shown which is colored according to the amplitudes of the membrane current source densities at a time instant. To visually enhance the current events, gray circles proportional to the amplitude of CSD at a point are placed centered at the point to facilitate comprehension.

3.2 Recording and pre-processing the experimental data

As a proof-of-concept of the skCSD method (Section 4.3), its performance was tested on experimental data. In this section the methods of the recording and data pre-processing is to be found.

In vitro experiment One male Wistar rat (300g) was used for the slice preparation procedure. The in vitro experiment was performed according to the EC Council Directive of November 24, 1986 (86/89/EEC) and all procedures were reviewed and approved by the local ethical committee and the Hungarian Central Government Office (license number: PEI/001/695-9/2015). The animal was anesthetized with isoflurane (0.2 ml/100g). Horizontal hippocampal slices of 500 m thickness were cut with a vibratome (VT1200s; Leica, Nussloch, Germany). We followed our experimental procedures developed for human in vitro recordings [Kerekes et al. 2014], adapted to rodent tissue. Briefly, slices were transferred to a dual superfusion chamber perfused with artificial cerebrospinal

fluid. Intracellular patch-clamp recordings, cell filling, visualization and three-dimensional reconstruction of the filled cell was performed as described in [Kerekes et al. 2014]. For the extracellular local field potential recordings, we used a 16-channel linear multielectrode (A16x1-2mm-50-177-A16, Neuronexus Technologies, Ann Arbor, MI, USA), with an INTAN RHD2000 FPGA-based acquisition system (InTan Technologies, Los Angeles, CA, USA). The system was connected to a laptop via USB 2.0. Wideband signals (0.1—7500 Hz) were recorded with a sampling frequency of 20 kHz and with 16-bit resolution. The recorded neuron was held by a constant -40 nA current injection.

Data pre-processing 154 spikes were detected on the 180s long intra-cellular recording by 0 mV upward threshold crossing. A 5 ms wide time windows were cut around the moments of each spikes on each channels of the extra-cellular (EC) potential recordings and averaged, to access the fine details of the EC spatio-temporal potential pattern which accompanied the firing of the recorded neuron on all channels. Two channels were broken (2, 5), however, as the skCSD method allows retrieving CSD maps from arbitrarily distributed contacts, this has not prevented the analysis; the broken channels were excluded from further consideration. The averaged spatio-temporal potential maps were high-pass filtered by subtracting a moving window average with 100 ms width. This filtering, together with the spike triggered averaging procedure, ensured that the resulted EC potential map contains only the contribution from the actually recorded cell. The price we paid was filtering out EC signals of the spontaneous repetitive sharp-wave like activity of the slice which was correlated by the firing of the recorded neuron and thus the presumptive synaptic inputs of the recorded neuron as well. An additional temporal smoothing by a moving average with 0.15 ms window was used to reduce the effect of noise.

DOI:10.14753/SE.2020.2264

4 Results

4.1 Results related to the existence of monopole sources

In order to check our hypothesis, the following steps were carried out:

1. Simulate extracellular potential of a firing cell on a 3D electrode grid and take various interelctrode distances, in order to see the change in the spatial sampling, for the same volume
2. Use tCSD and vCSD methods to calculate the current source distributions source distribution
3. Calculate the monopole, dipole and quadrupole moments for both tCSD and vCSD:

4.1.1 Description of the simulations

To validate the method we used simulated data which allows us to consider arbitrary cell-electrode setups and test various current patterns. The LFPy package [Lindén et al. 2014] was used to simulate the extracellular potential at arbitrarily placed virtual electrodes.

Y-shaped neuron In this investigation we started with a simple cell model, very similar to the one described in Paragraph 4.3.2.2, with the only difference, that the size of the cell was scaled up, but other parameters regarding the electrophysiological properties remained unchanged. The soma of the cell was placed to the (0,-800,0) position. The dimensions of the electrode grid was 1200 μm x 800μm x 1400 μm with interelectrode distances varying between 50, 100, 200 μm. A 2 dimensional projection of the setup is show on Figure 4.1.k, where the black circles represent the densest electrode grid setup and the shape of the cell is also shown.

Pyramidal neuron The electrodes were distributed in the same volume of 1200 μm x 800μm x 1400 μm, in the 3 different basic setups the interelectrode distances in all directions were 50, 100, 200 μm. In this case a CA3 pyramidal neuron [Ishizuka et al. 1995] was selected from the NeuroMorpho database for the electrophyisiological simulations. The simulation lasted for 70 ms, active channels were located only on the soma, passive channels as well as synapses were similarly distributed on the apical and basal dendrites. The *ExpSyn* synapse model was used with time constant $\tau = 2$ ms, synaptic weight: 0.01 μS, reversal potential: 0 mV. During the time of the simulation altogether 1000 synaptic

DOI:10.14753/SE.2020.2264

inputs arrived to 100 synapses, these were distributed randomly along the cell. More parameters of the simulation are to be found in Table 3.2.

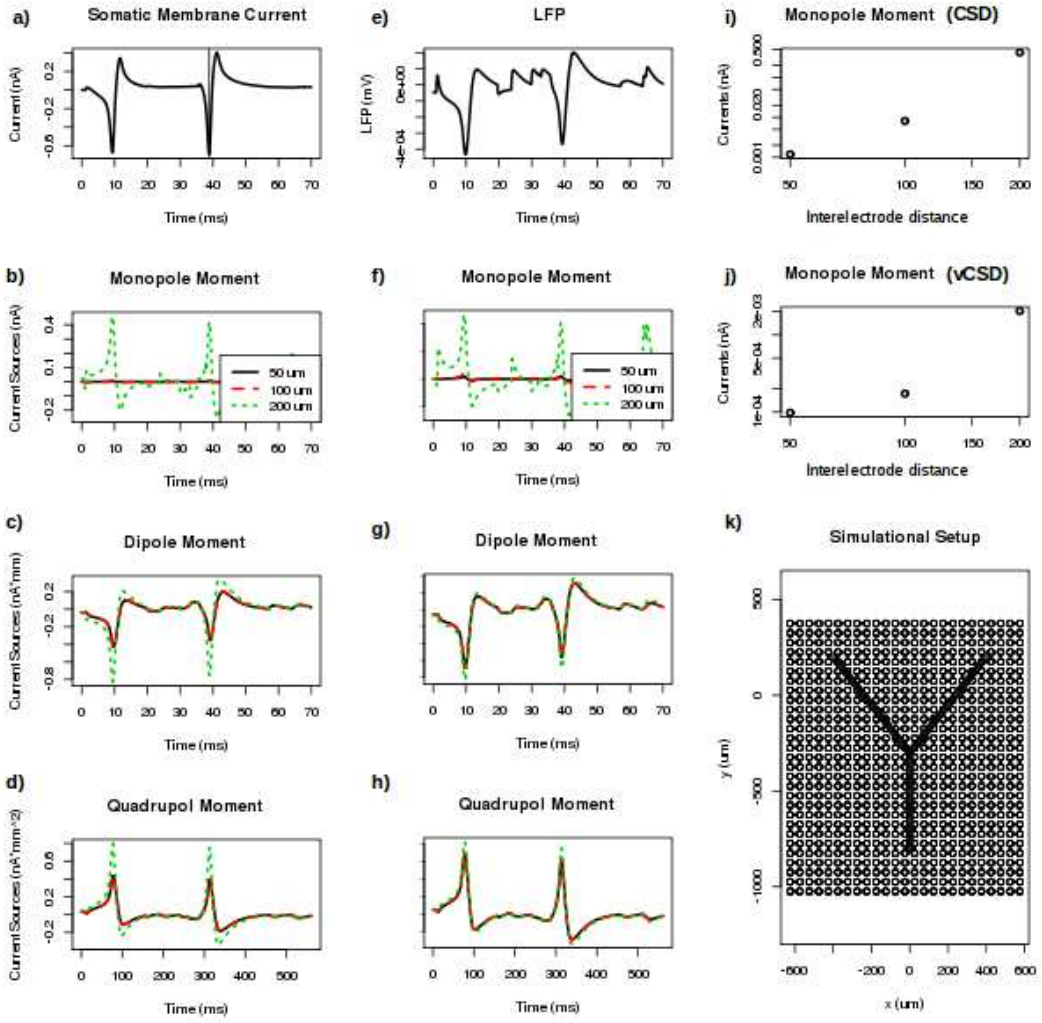

Figure 4.1: ***tCSD and vCSD reconstruction of simulated extracellular potential.*** *a) Somatic membrane current. The vertical line shows the time instant, when the current moments were compared on part f). b) CSD monopole current moments, where the colour indicate various interelectrode distances. c) CSD dipole moments. d) CSD quadrupol moments. e) Extracellular potential measured by the electrode placed nearest to the soma. f) vCSD monopole current moments, where the colours indicate various interelectrode distances. g) vCSD dipole moments. h) vCSD quadrupol moments. i) CSD monopole moments at the peak of spike as a function of the interelectrode distance. j) vCSD monopole moments at the peak of spike as a function of the interelectrode distance. k) Section of the simulational setup, where the circles mark the location of electrodes in case of 50 µm interelectrode distance and the black shape shows the morphology of the toy neuron.*

4.1.2 Calculation of current source density distributions

From the extracellular potentials retrieved from the simulation, the tCSD and vCSD can be calculated for each interelectrode distance. The regularization parameter for vCSD had the value of λ=100. The CSD values on the x-y planes closest to the soma for the Y-shaped cells are shown on Figures 4.2 and 4.3 for 50,100 and 200 μm interelectrode distances. Note, that as the vCSD method calculates to CSD values at the electrode grid points and the tCSD method at in between, in case of the same electrode setup used, it was only possible to show the values 25 μm apart from each other. Still, the effect of finite spatial sampling is clearly visible, the resolution gets worse and worse with the increase of the interelectode distance, the finite details are lost.

4.1.3 Calculation of the moments

The moments were calculated by using the following equations:

- Monopole moment:
$$M(t) = \sum I(\mathbf{r}), \tag{4.1}$$
where $M(t)$ is the the monopole moment at time t and $I(r)$ is the current in location r.

- Dipole moment:
$$D_y(t) = \sum I(\mathbf{r})(r_y - r_0), \tag{4.2}$$
where $D_y(t)$ is the the dipole moment for the y axis at time t and $r_y - r_0$ is y component of the position of the current source measured from the origo.

- Quadrupole moment:
$$Q_y(t) = \sum I(\mathbf{r})(r_y - r_0)^2 \tag{4.3}$$
where $Q_y(t)$ is the the quadrupole moment for the y axis.

Thereafter in order to get currents (I) from the current source density (C) at a point, each value was multiplied by the volume of the cube with the sides of the interelectode distances in case of tCSD. As in case of VCSD we calculated the current in each point of a grid with 50 μm grid constant, the CSD values were multiplied by $50^3 \mu m^3$.

4.1.4 Revealing the moments

For a more quantitative understanding, we plotted the monopole, dipole quadrupole moments for the 70 ms of the simulations for both vCSD and tCSD together with the

DOI:10.14753/SE.2020.2264

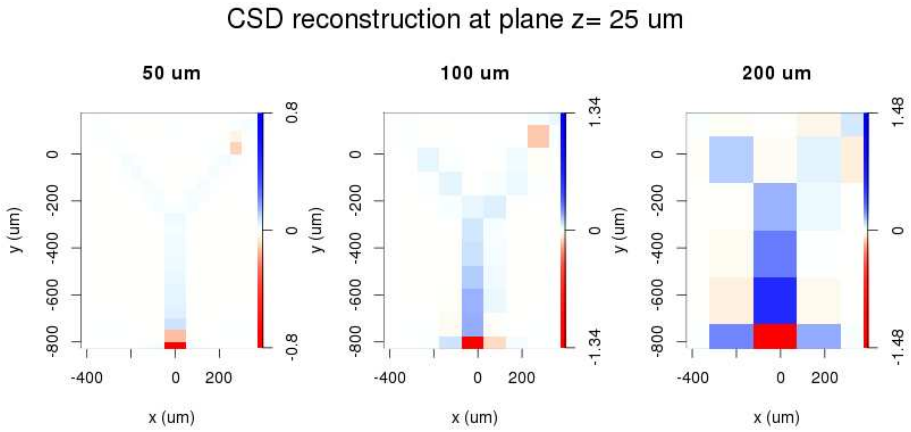

Figure 4.2: ***Reconstruction with the traditional CSD method at the plane 25 µm from the plane of the Y-shaped cell.*** *The interelectrode distance is increasing from left to right, which is inducing a reconstruction error.*

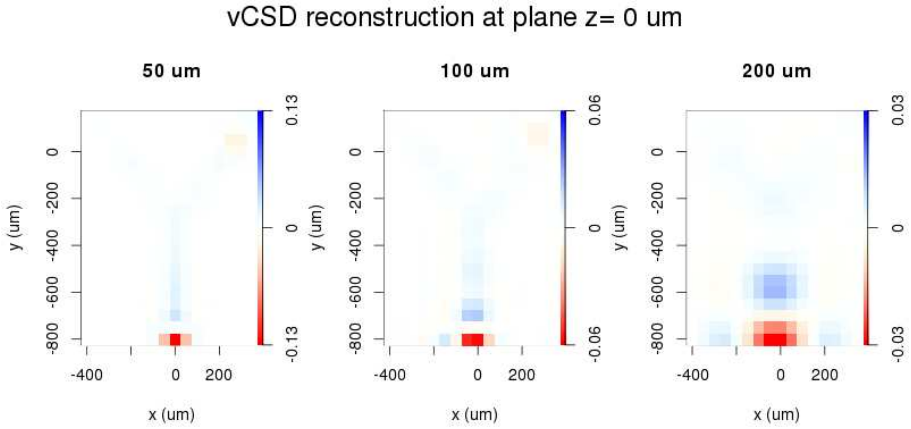

Figure 4.3: ***Reconstruction with the vCSD method at a plane of the Y-shaped cell by using the regularization parameter value 100 in each cases.*** *The reconstruction is distorted in a different way compared to CSD.*

somatic membrane current and measured extracellular potential by the electrode closest to the soma on Figure 4.1. Not surprisingly, the biggest deviation of the moments happens, when there are big changes in the membrane currents and so in the extracellular potential. When looking at the values of the monopole moment at the peak of the spike on Figure 4.1 i) and j), the tendency for both methods is the same, the better the resolution, the smaller the monopole moment is.

Furthermore as Figure 4.4 highlights, while the other moments are not that effected by the resolution, the apparent monopole moment highly depends on the interelectrode

DOI:10.14753/SE.2020.2264

distance. In order to get a more robust idea about the appearance of monopole, we considered the average monopole, dipole and quadrupole moment values for three experimental setups, where the electrode grid was shifted by 0, 5, 10, 15, 20, 25 μm in case of 50 μm grid constant , 0, 10, 20, 30, 40, 50 in case of 100 μm grid constant, 0, 20, 40, 60, 80, 100 in case of 100 μm grid constant MEAs respectively in the direction of z.

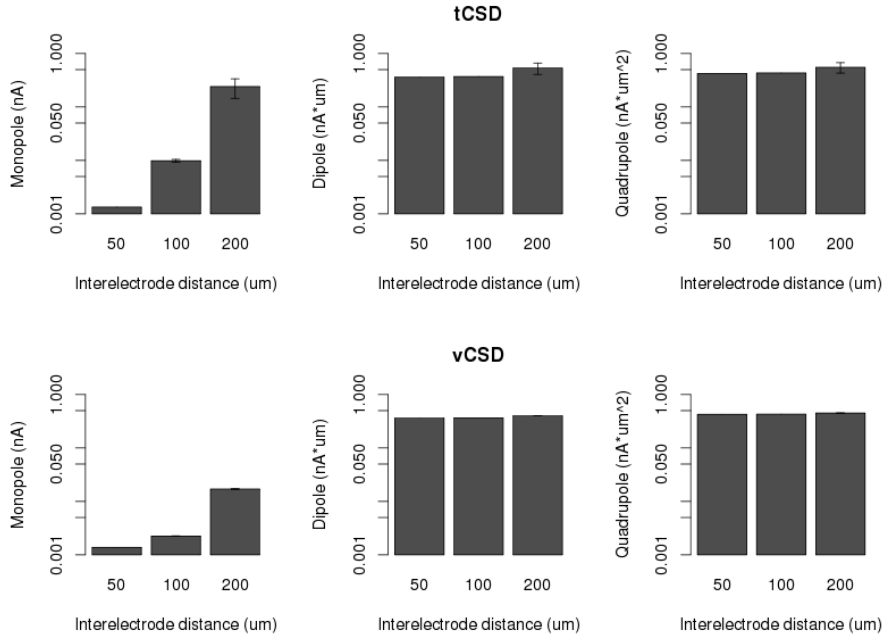

Figure 4.4: ***Monopole (left), dipole (middle) and quadrupole moments at the time of spiking activity in case of traditional CSD (above) and vCSD (below) reconstruction in case of the Y-shaped neuron model.*** *The value of monopole moment is highly dependent on the mesh size, a sparse electrode distribution induces bigger "measured" monopole.*

When using a more complicated cell morphology, this conclusion was strengthened. While the fine electrode grid captures the local changes of membrane current and extracellular potentials during the spike, when using a sparse electrode grids, all details are lost. The quantitative values presented on Figure 4.6 again support this findings.

DOI:10.14753/SE.2020.2264

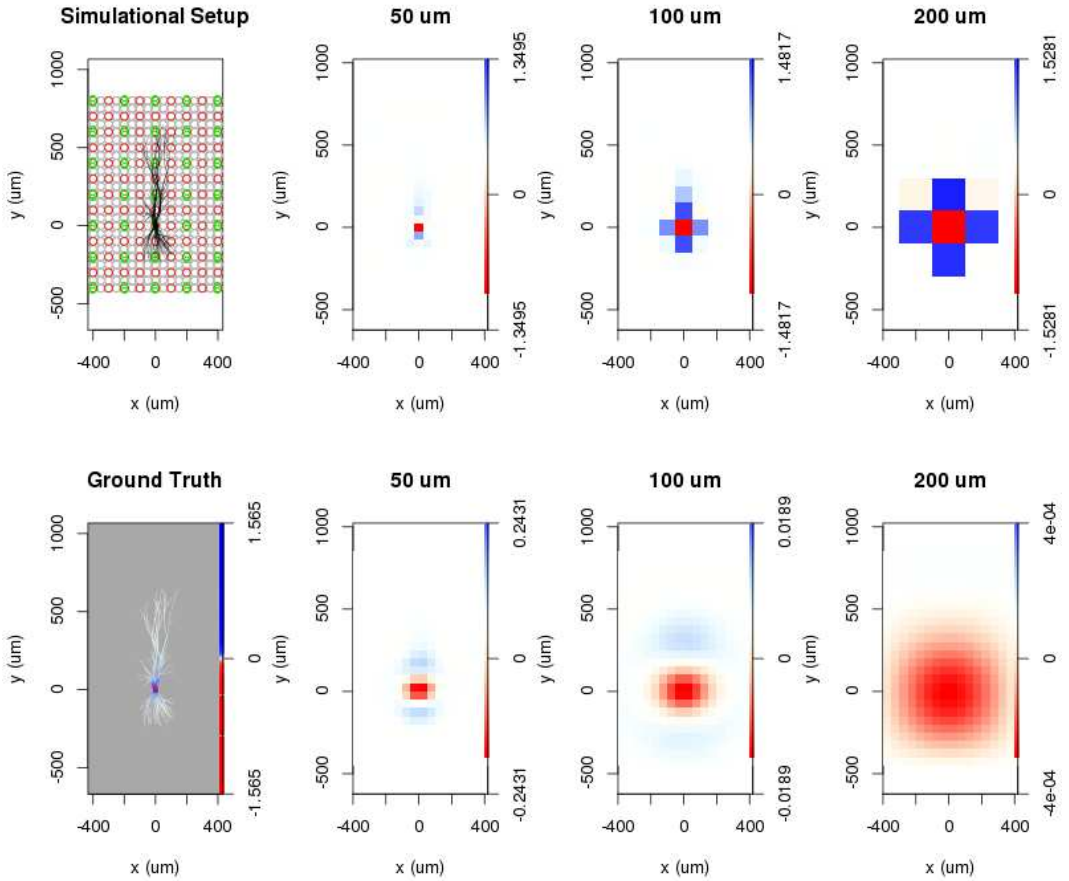

Figure 4.5: ***Simulational arrangement and visualization of the reconstructed current source distributions estimated by the traditional CSD and vCSD methods in the x-y plane in case of the pyramidal neuron model.*** *The 2 dimensional projections of the morphology of the cell is drawn in black, the position of the recording electrodes are marked by colored circles. According to the various interelectrode-distance, grey, red and green circles correspond to the 50, 100, 200 µm interelectrode-distances. The bottom left figure presents the ground truth membrane current density distribution, red indicates current sinks, blue current sources. The reconstruction with the traditional CSD is shown on the first row, with the vCSD in the second; the 2nd, 3rd and 4th column correspond to the usage of 50, 100, 200 µm interelectrode-distances. It is clearly visible that bigger interelectode-distances lead to the distortion of the details of the CSD distribution in case of both methods.*

4.2 Results related to the sensitivity of the sCSD method in case of a tilted cell

The main goal of this section is to present the result related to the investigation of an imperfect cell-electrode setup. There are numerous ways of how this can happen, we limit the studied scenarios to the case, when the cell is tilted with angles α, β and the distance

DOI:10.14753/SE.2020.2264

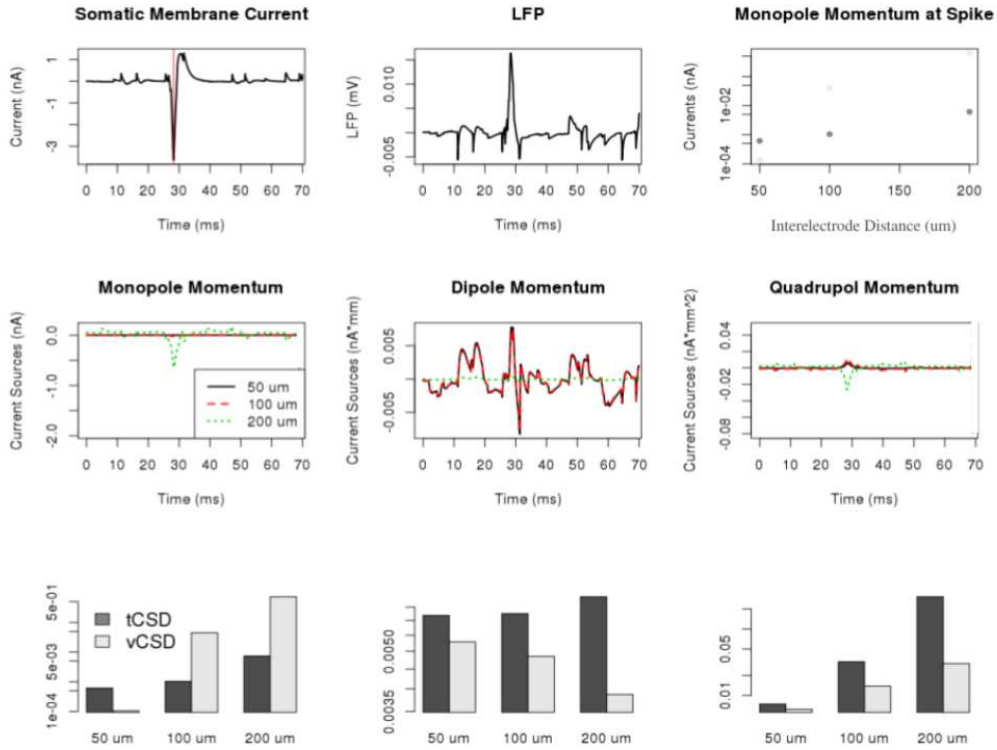

Figure 4.6: ***Quantitative analysis of CSD reconstructions in case of finite spatial sampling in case of the pyramidal neuron model.*** *The top left and middle figure show the ground truth somatic membrane current and extracellular potential on an electrode close to the soma. The red line indicates the peak of the spike, the monopole-, dipole- and quadrupole moments calculated with the traditional CSD (dark grey dots) and vCSD (light grey dots) at this moment are shown on the top right figure. The detailed temporal course for the vCSD method in case of all interelectrode distances are shown in the second row. The same quantities are shown in the 3rd row at the the peak of the spike. The standard deviations on the error bars were calculated from averaging the absolute value of moments in the reconstructions in case of shifting electrodes with one-tenth, two-tenth and three-tenth of the interelectrode distances.*

of the soma is d from the electrode as shown in Fig. 2.1.

Simulation of ground truth data A ground truth CSD distribution, which is similar to one when firing, was generated as 160 point sources 10 μm apart from each other, as shown on Fig. 4.7. The distribution was dominated by a large, point-like sink with an amplitude of 1. The counter currents were symmetric and decayed exponentially as the distance from the soma. A Gaussian-shaped positive current was added to the first branch of. The relative amplitude of these dendritic currents was as small as 1-3 % of the main sink, but in accordance with zero sum requirement, the sums of the currents along the line sources were set to zero in all the three cases.

DOI:10.14753/SE.2020.2264

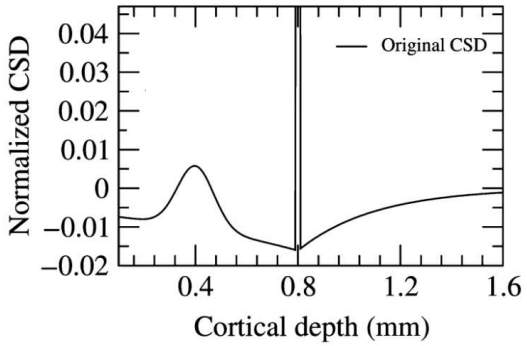

Figure 4.7: ***Ground truth CSD distribution for analyzing the effect of a setup, in case the cell is not completely parallel to the electrode.*** *The amplitudes of the main sinks are normalized to 1, but the graph in the is cut in order to make visible the differences of the small-amplitude counter currents.*

The extracellular potentials were calculated as a superposition of the potential of the point sources,which were distributed on the axis of the cells. The axis of the cell was tilted with angles α $[0°, 10°, ..., 60°]$, $\beta [0°, 45°, 90°]$, the soma to electrode distance was d $[20\mu m, 40\mu m, 60\mu m]$. Tilt towards the electrode within a common plane is denoted by $\beta = 0°$ and the tilt perpendicular to the cell–electrode direction is denoted by $\beta = 90°$.

Findings Fig. 4.8 shows how the precision of the CSD reconstruction and the distance estimation depends on the relative angle of cell and the electrode. It was found, that the smaller details of the original CSD diminished on the reconstruction with the increasing tilt, but no spurious sources appeared on the sides of the main sink, which was typical for the tCSD (Fig. 4.8, top row). Parallel, the reconstruction error increased slightly for the sCSD with the increasing tilt, but the RMSE remained lower for sCSD than for tCSD for all α, β and distance combinations (Fig. 4.8, middle row). As the tilt increased, the originally equal distances between different parts of the cell and the line of the electrode became different. This effect is most pronounced in case of $\beta = 0°$, thus the reconstruction deteriorates most rapidly in this direction. In these non-parallel cases, we defined the cell–electrode distance as the distance between the soma and the probe, and compared the sCSD distance estimations to it (Fig. 6, bottom row). The distance estimation was relatively insensitive to the tilt for $\beta = 90°$ and 45° cases, but $\beta = 0°$ results in rapid increase in the distance estimation error with the increasing tilt. Even in this worst case, distance estimation error remained under 20 μm up to $= 20°$ for all examined distances (d =20, 40, 60 μm), thus we concluded, that the distance estimation gives reasonable results up to $= 20°$ deviation for any case.

DOI:10.14753/SE.2020.2264

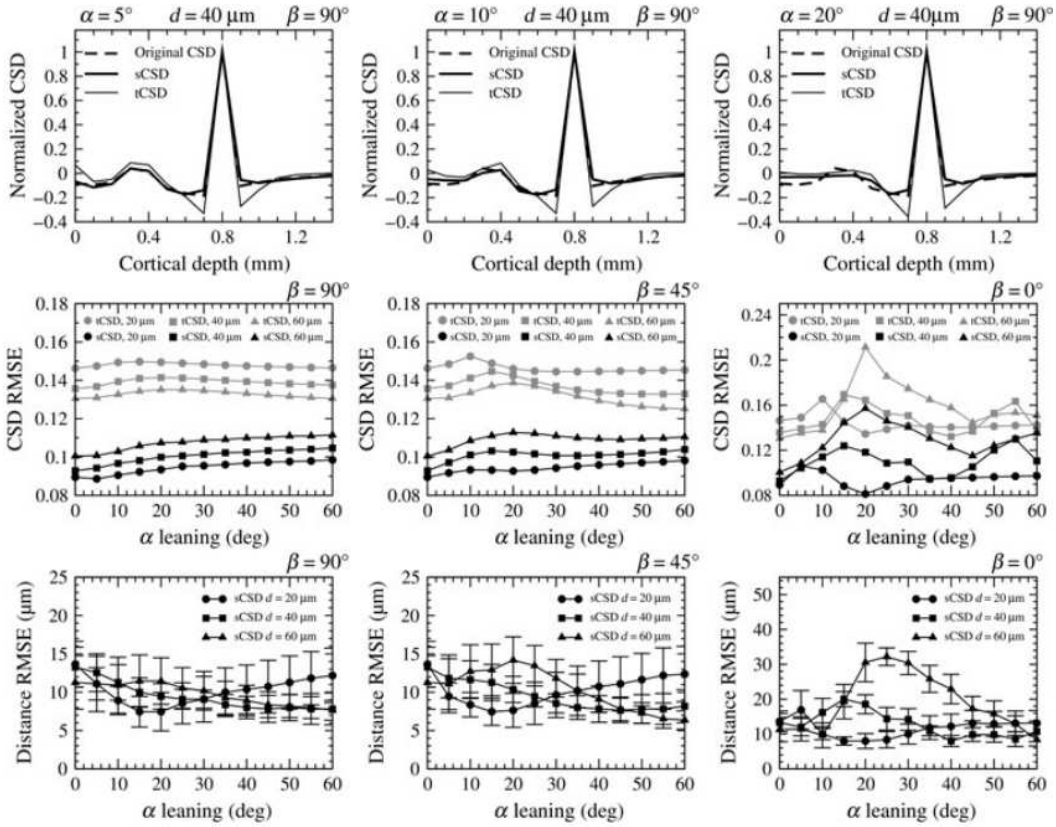

Figure 4.8: ***Test of CSD sensitivity to the angular deviation between the cell and the electrode.*** *α denotes the deviation from the parallel and β denotes the direction of the deviation. $\beta = 90°$ means, that the deviation is perpendicular to the cell–electrode direction, while $\beta = 0°$ marks cell leaning towards the electrode. First row: comparison of sCSD and tCSD reconstruction on examples with increasing leaning from $\alpha = 5°$ to $\alpha = 20°$. CSD methods were applied on V patterns calculated from source shown in Fig. 4.7. The small details diminished with the increased leaning. Middle row: leaning dependency of the average CSD reconstruction error in three different leaning directions and distances. While error increases with the increasing leaning (most rapidly for $\beta = 0°$), sCSD resulted in smaller error for all cases. The root mean square error (RMSE) values are averages over the 10 different electrode–soma relative positions. Bottom row: leaning dependency of the distance estimation error. Mean errors and the standard error of means are shown. The distance estimation is relatively insensitive in $\beta = 90°$ and $\beta = 45°$ cases, but $\beta = 0°$ results in a rapid increase in the distance estimation error. Note the different scale for $\beta = 0°$.*

4.3 Results related to the skCSD Method

4.3.1 Main result regarding the skCSD method

The main result of this work is the introduction of the skCSD method, so we start here with the developement of the theoretical framework. Next, we study the properties of the skCSD reconstruction for three representative morphologies of increasing complexity and

for different setups.

First, for a ball-and-stick neuron, we study the general quality of reconstruction of fine detail by considering CSD distributions in the form of standing waves of increasing spatial frequency which form the Fourier basis of any possible CSD profile. It is unlikely that standing waves would be naturally observed in a cell, therefore, to better understand how the results for the Fourier space representation relate to a specific distribution which might arise in a physiological situation, we also consider reconstruction of sources for random synaptic activation of the ball-and-stick cell.

Secondly we consider a Y-shaped neuron with a single branching point, we check if skCSD can differentiate between synaptic activation located on the different branches close to the branching point. We also investigate the effects of random distribution of contacts on skCSD reconstruction. Finally, we investigate the possibility of skCSD reconstruction on a realistic model of a ganglion cell placed on a microelectrode array (MEA) as well as the sensitivity of the method to noise.

After establishing and validating skCSD on these fully controlled model datasets, to demonstrate neurophysiological viability, the CSD distribution was reconstructed for a pyramidal cell using the experimental spike-triggered averages of the recorded potentials.

4.3.2 Theoretical framework

The single cell kCSD method (skCSD), which we introduce in this work, is an application of the kCSD framework where we assume that the measured extracellular potential comes mainly from a cell of known morphology and known spatial relation to the MEA. To estimate the CSD in this case we must cover the morphology of the cell with a collection of basis functions. To do this, a one dimensional parametrization of the cell morphology is needed. This could be done independently for each branch of the neuron or globally for the whole cell at once. While the first approach might seem easier, handling of the branching point is non-trivial. Instead, we decided to fit a closed curve on the morphology, which we call the *morphology loop* (Fig. 4.9). This curve should cover all the segments of the cell, be as short as possible, and be aligned with the morphology. For example, in case of a ball-and-stick neuron, the curve starts at the soma, goes towards the tip of the dendrite, turns back, goes back to the soma, and closes there. One parameter s is enough to unambiguously determine a position on this line, although most points on the morphology are mapped to two s parameters. We also need a method to handle the branching points and guide the parametrization so that all the branches will be visited in an optimal way. This problem is a special case of the Chinese postman problem known from graph theory [Kwan 1962]. Given this information we can distribute the basis functions $\widetilde{b}_j(\mathbf{x})$ along the morphology of the cell (Fig. 4.9).

DOI:10.14753/SE.2020.2264

In practice, based on the morphology information we define an ordered sequence of all the segments such that the consecutive segments are always physically connected and preference is given to those neighbors which have not been visited yet. The process is continued until all the segments are covered and the last element in the sequence connects to the first element. Note that in the sequence the final segments of the branches are present once, the branching point multiple times and the intermediate ones twice. Then we fit a spline on the coordinates of the segments following the ordered sequence resulting in a morphology loop construction. The CSD basis functions are distributed along this loop uniformly. Any point $\mathbf{x} \equiv (x, y, z)$ on the morphology can be parameterized with $s \in [0, l]$ on the loop:

$$\begin{aligned} x &= f_x(s), \\ y &= f_y(s), \\ z &= f_z(s), \end{aligned} \tag{4.4}$$

where l is twice the length of all the branches. Consider the following basis functions:

$$\widetilde{b}_i(s) = e^{-(s-s_i)^2/R^2} \tag{4.5}$$

where s_i is the location of the i-th basis function on the morphology loop, R its width.

The contribution to the extracellular potential from a basis source $\widetilde{b}_i(s)$ is given by

$$b_i(x,y,z) = \frac{1}{4\pi\sigma} \int \frac{\widetilde{b}_i(s)}{\sqrt{(x-f_x(s))^2 + (y-f_y(s))^2 + (z-f_z(s))^2}} ds. \tag{4.6}$$

As in kCSD, for CSD of the form

$$C(s) = \sum_{i=1}^{M} a_i \widetilde{b}_i(s)$$

we obtain the extracellular potential as

$$V(\mathbf{x}) = \sum_{i=1}^{M} a_i b_i(\mathbf{x}). \tag{4.7}$$

As before, for estimation of potential we use kernel interpolation. Note that in this case the basis functions in the CSD space, $\widetilde{b}(s)$, live on the morphology loop, while the basis functions in the potential space, $b_i(\mathbf{x})$, live in the physical 3D space. To determine the current source density distribution along the fitted curve we introduce the following kernel

functions:

$$K(\mathbf{x},\mathbf{x}') = \sum_{j=1}^{M} b_j(\mathbf{x}) b_j(\mathbf{x}'), \tag{4.8}$$

$$\widetilde{K}^T(s,\mathbf{x}') = \sum_{j=1}^{M} \widetilde{b}_j(s) b_j(\mathbf{x}'). \tag{4.9}$$

With these definitions the regularized solution for C on the morphology loop is given by Eq. (3.15):

$$\mathbf{C}(s) = \widetilde{\mathbf{K}}^T(s)(\mathbf{K} + \lambda \mathbf{I})^{-1}\mathbf{V}. \tag{4.10}$$

To obtain the distribution of currents at a given point in space we need to sum the currents on the loop at points which are mapped to that physical position $\mathbf{x}$:

$$\mathbf{C}(\mathbf{x}) = \sum_{s:r(s)=\mathbf{x}} \mathbf{C}(s). \tag{4.11}$$

4.3.2.1 Ball-and-stick neuron

Here we consider the simplest neuron morphology, the so-called ball-and-stick model, which stands for the soma and a single dendrite. A virtual linear electrode was placed in parallel to the model cell 50 μm away, the contact points were distributed evenly along the electrode extending for 600 μm.

Increasing the density and number of electrodes improves spatial resolution of the method To study the spatial resolution of the skCSD method we consider the ground truth membrane current source density distributions in the form of waves with increasing spatial frequencies

$$CSD(x) = A\cos(2\pi f x/L),$$

where $A = 0.15\ nA/\mu m$ is the amplitude, $f \in \{0.5, 1, 1.5, \ldots, 12.5\}$ is the spatial frequency, x is the position along the cell, L is the length of the cell. Then, we compute the generated extracellular potential at the electrode locations. The laminar shank consisting of 8, 16 and 128 electrodes was placed 50 μm from the cell in parallel to the dendrite. Finite sampling of the extracellular space sets a limit to the spatial resolution of this method. Increasing the density of electrodes within the studied region leads to higher spatial precision. As shown in Fig. 4.10, with 128 electrodes it is possible to reconstruct higher frequency distributions as compared to 8 electrodes. This is reminiscent of the sampling theorem [Nyquist 1928], except here we measure the potential and reconstruct current sources, while in the sampling theorem we consider the reconstruction of a continuous signal from

DOI:10.14753/SE.2020.2264

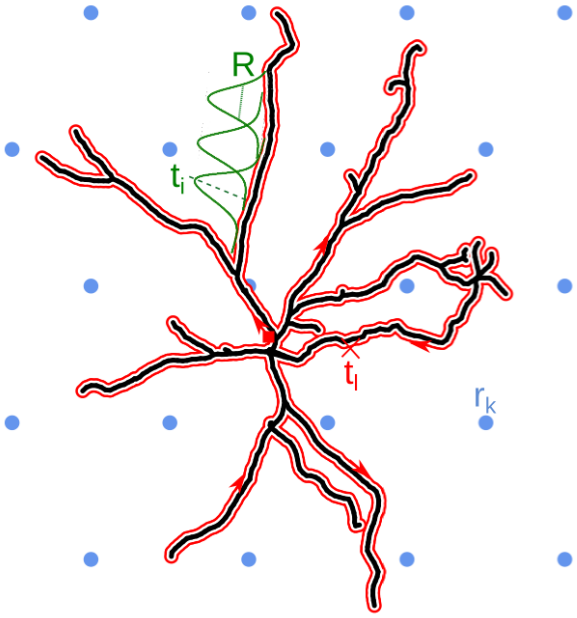

Figure 4.9: ***Schematic overview of the skCSD method.*** *The black line indicates the 2-dimensional projection of the neuron on the MEA plane, the blue circles mark the location of multielectrode array (hexagonal grid, in this example),* r_k *is the position of the* k^{th} *electrode. The morphology in our method is described by a self-closing curve in three dimensions, which is indicated by red on the plot. We shall refer to this curve as the* morphology loop*. A point of the cell is visited once, if it is a terminal point of a dendrite, more than twice, if it is a branching point and twice in all the other cases. With this strategy, any point on the morphology loop uniquely identifies the physical location of the corresponding part of the cell unambiguously. To set up estimation framework we distribute 1-dimensional, overlapping Gaussian basis functions spanning the current sources. Several of these Gaussians are plotted in green,* t_i *marks the center of the* i^{th} *basis element, R is the width parameter.*

discrete samples. What we observe is quite intuitive and typically observed in different discrete inverse methods [*Discrete Inverse Problems*]. Note that once we move to complex morphologies and random rather than regular electrode placement, the intuition we build here, that denser probing gives better spatial resolution, would hold true, even if the relation to the sampling theorem would be less apparent.

DOI:10.14753/SE.2020.2264

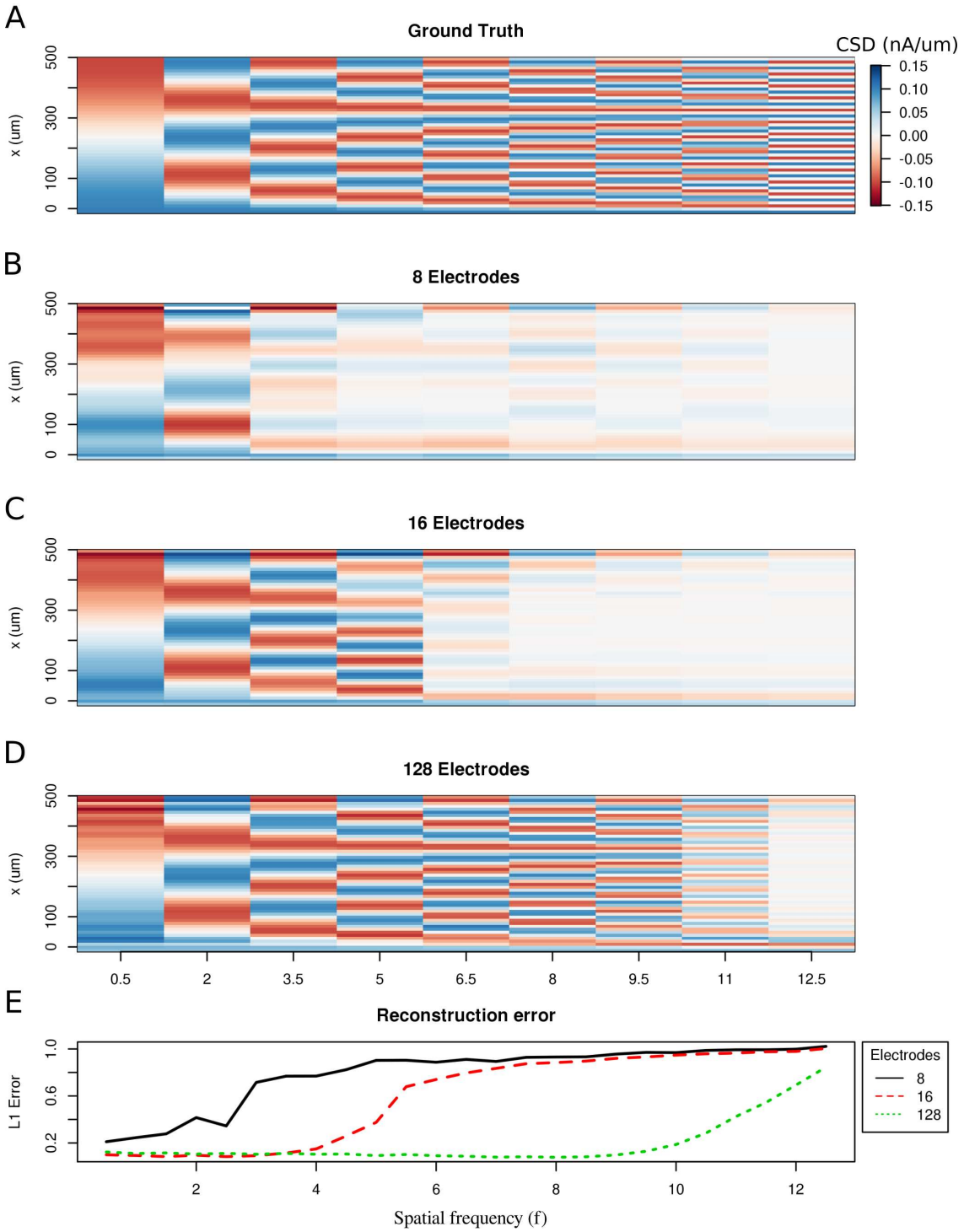

Figure 4.10: ***Limitations of the spatial resolution of the skCSD method in a simple ball-and-stick and laminar electrode setup.*** ***A****. The ground truth membrane current source density distribution was constructed from cosine waves of increasing spatial frequency (x-axis) along the cell mophology (y-axis), which is shown in the interval representation.* ***B–D****. skCSD reconstruction from 8, 16 and 128 electrodes.* ***E****. The L1 norm error of the skCSD reconstruction for 8 (black), 16 (red) and 128 (green) electrodes for CSD patterns of increasing frequency.*

Reconstruction of random synaptic activation Using the ball-and-stick neuron we now place 100 synapses along the dendrite and stimulate them randomly in time. We simulate 70 ms of recordings from this synaptically activated cell. The stimulation is sufficiently strong to evoke spiking. The spiking is indicated by strong red spots in the lowest first two segments in Fig. 4.11, which correspond to the soma. As can be seen, the reconstructed CSD distribution reflects the ground-truth, and the precision of reconstruction improves with an increasing number of contacts, which is reflected in the reduction of leave-one-out cross-validation error. Notice how the reconstructed synaptic activity gets more precise with increased density of probing the potential. In particular, observe how the width of the recovered synaptic and the somatic activation shrink with an increasing number of electrodes, which clearly shows improved resolution. This is consistent with our observations for the Fourier mode CSD profiles above. Not much change is seen in time, which is a consequence of the fact that skCSD, like all the CSD estimation methods, acts locally in time. That is, for every moment in time, the collection of potentials at this time, is analyzed. There is no direct relation to the past or future of the measured signals.

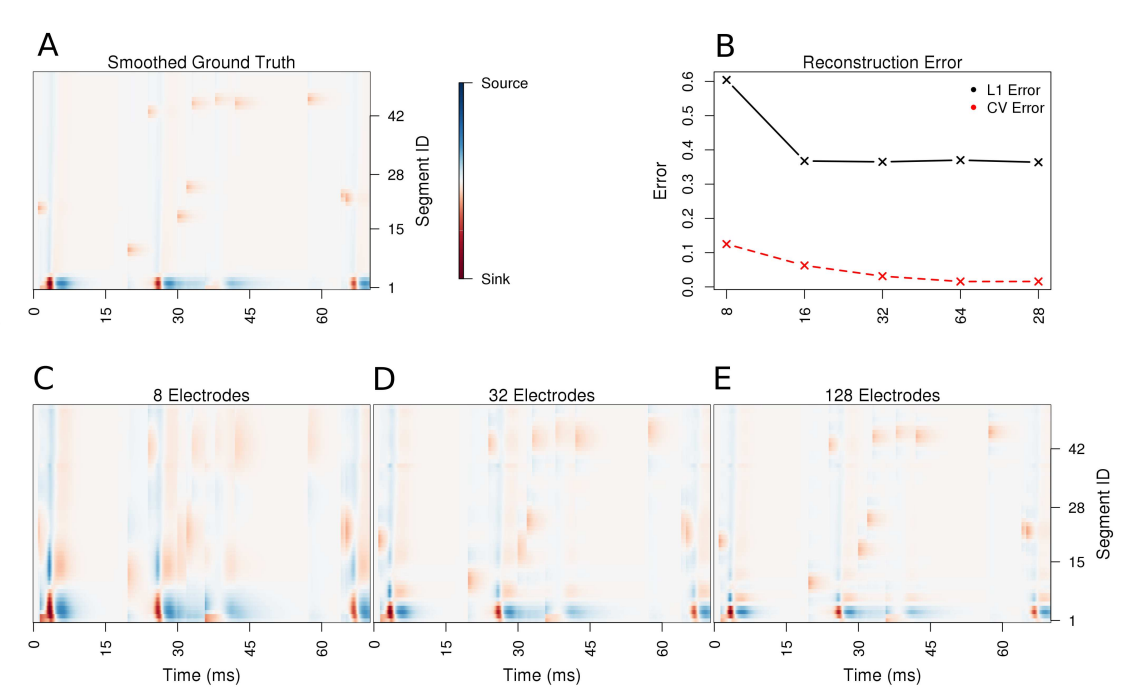

Figure 4.11: ***Performance of the skCSD method for a ball-and-stick neuron with random synaptic stimulation for recordings with a laminar probe placed 50 µm away from the cell. A****. The ground truth spatio-temporal membrane current density in time (x-axis) along the cell in the interval representation (y-axis). The lowest segment is the soma, where the visible high amplitude of potential is a consequence of spiking. To make the much less pronounced synaptic activity on the dendritic part visible, nonlinear color map was used. Panel* ***B*** *shows the lowest values of leave-one-out cross-validation and L1 norm error for the before-mentioned setups. Panels* ***C–E*** *present the best skCSD reconstruction in case of recording with 8, 32, and 128 electrodes. One can see how increasing the number and density of probes in the region improves the reconstruction quality until a certain level. CV error was used here to select the parameters leading to the best reconstructions.*

4.3.2.2 Simple branching morphology

Let us now study the effect of branching and breaking of rotational symmetry of the cell using the skCSD method. We consider here a simple Y-shaped model neuron with one branching point (Fig. 3.2 B). We place two synapses, one on each branch (at segments 33 and 62, close to the branching point, see Fig. 3.2 D and Fig. 4.12 C). We consider both simultaneous and independent activation of these synapses, specifically, the first synapse was activated at 5, 45, 60 ms of the 70 ms long simulation, while the other was stimulated at 5, 25, 60 ms from the stimulation onset. Our goals were to determine whether it was possible to separate the synaptic inputs located on two different branches, what happens at the branching point, how the arrangement of the electrodes-cell setup influences the reconstruction. We also wanted to determine whether this method provides

more detail about the current distribution on the cell than what is accessible from the interpolated potential and the CSD reconstructed with kCSD under the assumption of a smooth distribution of sources in space, which is the natural approach to try [Frey et al. 2009].

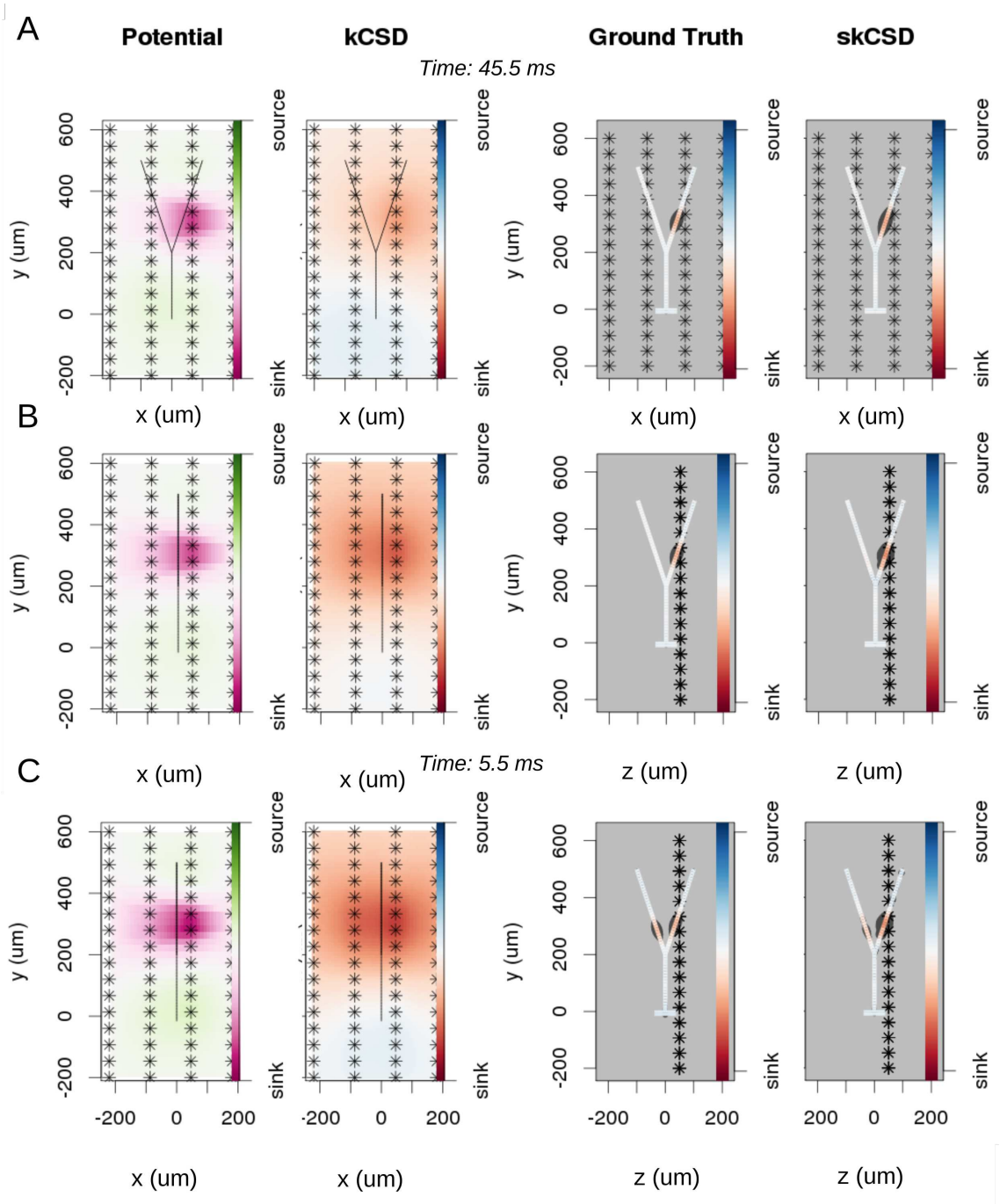

Figure 4.12: **Reconstruction of synaptic inputs on a Y-shaped neuron with a regular rectangular 4x16 electrode grid.** *Description on the next page.*

Figure 4.12: **Reconstruction of synaptic inputs on a Y-shaped neuron with a regular rectangular 4x16 electrode grid.** *Each panel (**A–C**) shows the spline-interpolated extracellular potential (V), followed by standard kCSD reconstruction, both at the plane of the 4x16 electrodes' grid used for simulated measurement. Then, the ground truth and skCSD reconstruction are shown in the branching morphology representation in the plane containing the cell morphology. Each figure shows the superimposed morphology of the cell. Note that in panel **A** the grid is parallel to the cell, while in panels **B–C** it is perpendicular. The dark gray shapes are guides for the eye and are sums of circles placed along the morphology with radius proportional to the amplitude of the sources at the center of the circle. **A**. Shows results for a synaptic input depolarizing one branch. **B**. Shows the same current distribution as in the previous setup, but the grid is rotated by 90 degrees. **C** A synaptic input is added to the other branch. Observe that in all three cases the interpolated potential and the standard CSD reconstruction, which can be drawn only in the plane of the electrodes' grid, do not differ significantly, hence they cannot distinguish between these three situations. On the other hand, skCSD method is able to identify correctly both synaptic inputs.*

Differentiation of synaptic inputs located on different branches To investigate the differentiation power of the proposed approach we consider two placements of the cell with respect to the electrode grid. Plane *xy*, in which the cell is placed in parallel to the plane of electrodes $50\mu m$ above (Fig. 4.12 A), and plane *xz*, where the cell is perpendicular to the grid, with the grid $50\mu m$ away from the dendritic shaft stemming from the soma, (Fig. 4.12 B, C). In Fig. 4.12, each panel (A–C) shows the spline-interpolated extracellular potential (V), followed by standard kCSD reconstruction, both at the plane of the 4x16 electrode grid used for simulated measurement. Then, the ground truth and skCSD reconstruction are shown in the branching morphology representation in the plane containing the cell morphology. Each figure is superimposed with the morphology of the cell. The dark gray shapes are guides for the eye and are sums of circles placed along the morphology with a radius proportional to the amplitude of the sources located at the center of the circle. Panel A shows results for a synaptic input depolarizing one branch. Panel B shows the same current distribution as in the previous setup, but the cell is rotated by 90 degrees with respect to the grid. In panel C synaptic input is added to the other branch. Observe that in all three cases the interpolated potential and the standard CSD reconstruction, which can be drawn only in the plane of the electrode grid, do not differ significantly, hence they cannot distinguish between these three situations. On the other hand, the skCSD method correctly identified the synaptic inputs in all three cases.

Note that without the method proposed here, the most natural approach to analyze current sources is through use of the regular, population CSD. This approach was used, for example, to investigate the changing distribution of current sources during action potential generation using data from a high-definition MEA [Frey et al. 2009]. What we show

in figures here and below, is that while CSD (kCSD) and skCSD are consistent, using the additional information about morphology renders significantly more detail about the activity studied.

The effect of electrode placement on skCSD reconstruction for Y-shaped cell In Fig. 4.13 we show how the number and specific distribution of the electrodes affect the quality of the reconstruction in the case of simultaneous stimulation. We considered 5 different, randomly generated version of electrode setups in case of each number of electrodes. Panel 4.13. A shows the ground truth data, that is the actual distribution of the transmembrane current sources, along the morphology. To visualize it simply, we used the interval representation, the soma is shown first, followed by one branch, followed by the other. Fig. 4.13.B shows the reconstruction results for regularly arranged 8 (4x2), 16 (4x4), 32 (4x8), and 64 (4x16) electrodes. In Fig 4.13.C we show reconstructions for five different random placements of the same number of electrodes as for the regular case. As expected, the skCSD method is able to recover the synaptic activation and the reconstruction resolution increases with the number of electrodes. Note that in certain cases the random distribution is more efficient than the regular grid, which is probably due to more fortunate samplings of the area covered by the morphology.

DOI:10.14753/SE.2020.2264

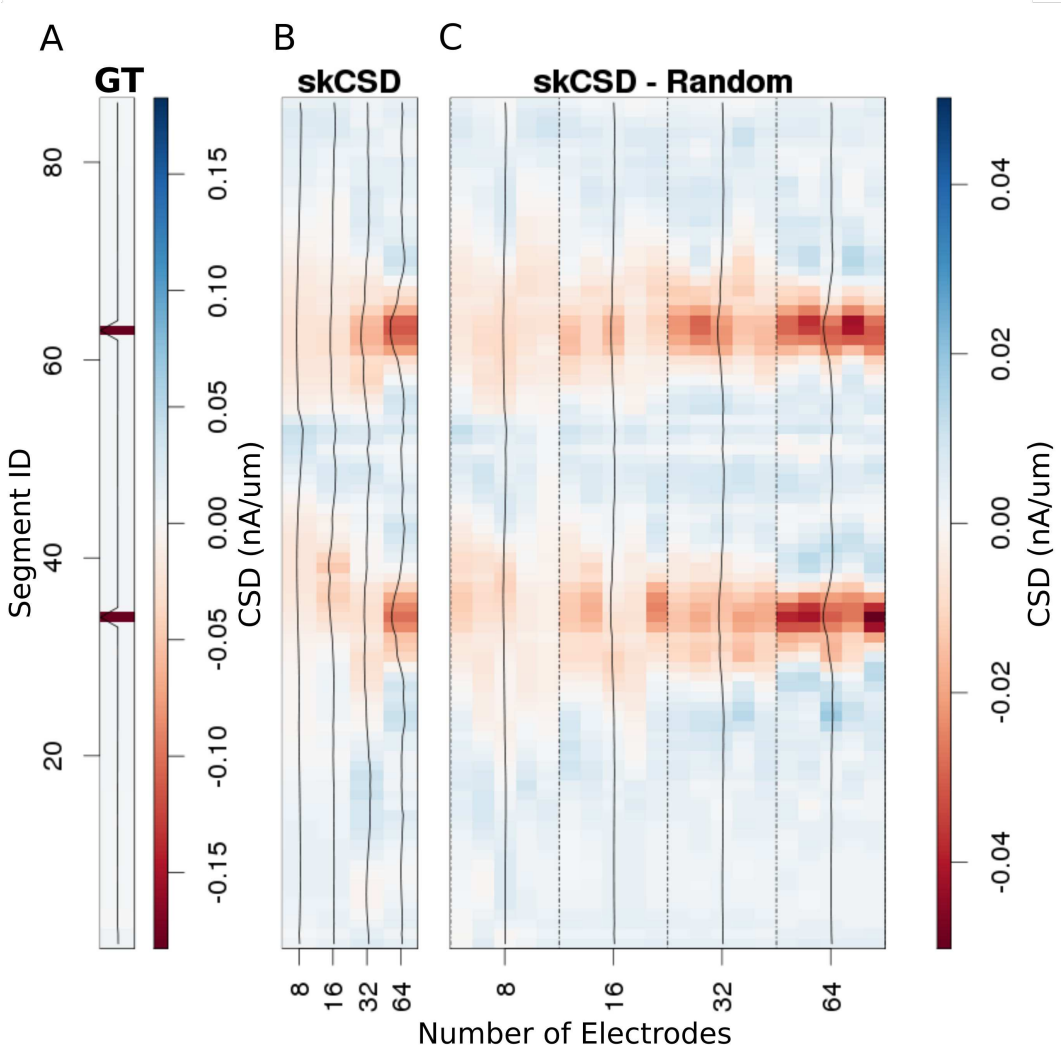

Figure 4.13: ***Reconstruction of synaptic inputs placed on different branches of the Y-shaped neuron for electrodes arranged regularly and randomly within the same area.*** *We use the interval representation for visualization. The numbers on horizontal axis enumerate different electrode setups. The black profiles show the averaged membrane current as reconstructed in a given case; for random electrode distribution these are averages over five different realizations.* ***A*** *Ground truth membrane currents, the strong red indicates the synaptic inputs.* ***B*** *Reconstruction results for 8 (4x2), 16 (4x4), 32 (4x8), and 64 (4x16) electrodes arranged regularly. The skCSD reconstruction improves with the number of electrodes as the color representation and the black profiles indicate.* ***C*** *When distributing the same numbers of electrodes on the same plane as in the previous case, the quality of the average skCSD reconstruction, as indicated by the black profiles, is similar.*

The effect of the choice of basis on skCSD reconstruction for the Y-shaped cell To investigate the reconstruction quality in the parameter space set by the number of basis functions (M), basis function width (R) and regularization parameter (λ), we used the simulation setup for the Y-shaped morphology with 4x4 electrodes. Fig. 4.14 shows the L1 norm reconstruction error for $M = 32, 128, 512, 1024$, $R = 8, 16, 32, 64, 128$, and

$\lambda = 1e-5, 1e-4, 1e-3, 1e-2, 1e-1$. As we can see, for the smallest basis ($M = 32$) and small λ, the minimum error is obtained for wide basis sources, so that the basis functions have substantial overlap. This is necessary for the method to be able to reconstruct the family of test sources we considered. As the basis size increases, the reconstruction improves overall with minimum error obtained for narrow basis sources and small λ. The fact that we have two comparable minima for $M = 32$, for small and large λ (top and bottom right of the plot for $M = 32$), means that the error we obtain by emphasizing the measurements (small λ) is comparable to the error we obtain by emphasizing the regularization term, which prevents over-fitting (large λ) and in effect, reflects our doubt about precision of measurement. We interpret it here as the effect of insufficient basis size. This effect disappears with increasing basis size when a unique minimum appears for moderate values of λ and for narrow basis sources, which can best resolve small details of the CSD to be reconstructed.

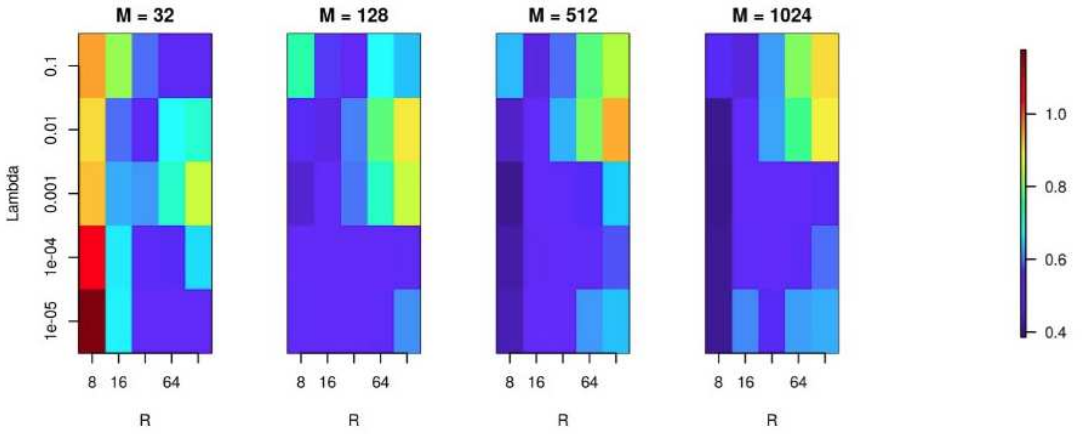

Figure 4.14: ***The effects of basis properties on reconstruction quality.*** *We used the Y-shaped morphology and the 4x4 electrode setup to investigate the effect of using various basis numbers for the reconstruction. L1 norm error was calculated to compare the results for basis with $M = 32, 128, 512, 1024$ elements, for several values of basis width R and λ. With few basis sources one cannot recover CSD properly. As the number of basis functions increases, the reconstruction error is minimized for moderate values of λ and for narrow basis sources, which can best resolve small details of the CSD to be reconstructed.*

4.3.2.3 Reconstruction of current distribution on complex morphology

In this section we consider the performance of the skCSD method in the case of a complicated, biologically realistic scenario. To achieve good spatial resolution, permitting detailed study of a cell with substantial extent, densely packed electrode arrays are required. In the present reconstruction we assumed a hexagonal grid arrangement with 17.5 μm inter-electrode distance inspired by recent experiments on reconstructing axonal action potential propagation [Bakkum et al. 2013; Frey et al. 2009]. We assumed a grid consisting

of 936 contacts from which we used 128 for reconstruction to be consistent with the hardware of [Bakkum et al. (2013) and Frey et al. (2009)].

In the simulation we assumed an experimentally plausible scenario, where oscillatory current was injected to the soma of a neuron in a slice with other inputs impinging through a 100 excitatory synapses distributed on the dendritic tree. The simulated data consisted of two parts. During the first 400 ms the cell was stimulated by the injected current as well as through the synapses. The amplitude of the injected current was 3.6 nA, the frequency of the current drive was around 6.5 Hz. During the second 400 ms the cell was stimulated only with the current. Fig. 4.15 shows an example of the skCSD reconstruction at a time selected right after a spike was elicited by the cell. As we can see, neither the standard CSD reconstruction assuming smooth current distribution in space, nor the interpolated potential, recover to the actual current distribution. At the same time, the skCSD reconstruction is quite a faithful reproduction of the ground truth.

DOI:10.14753/SE.2020.2264

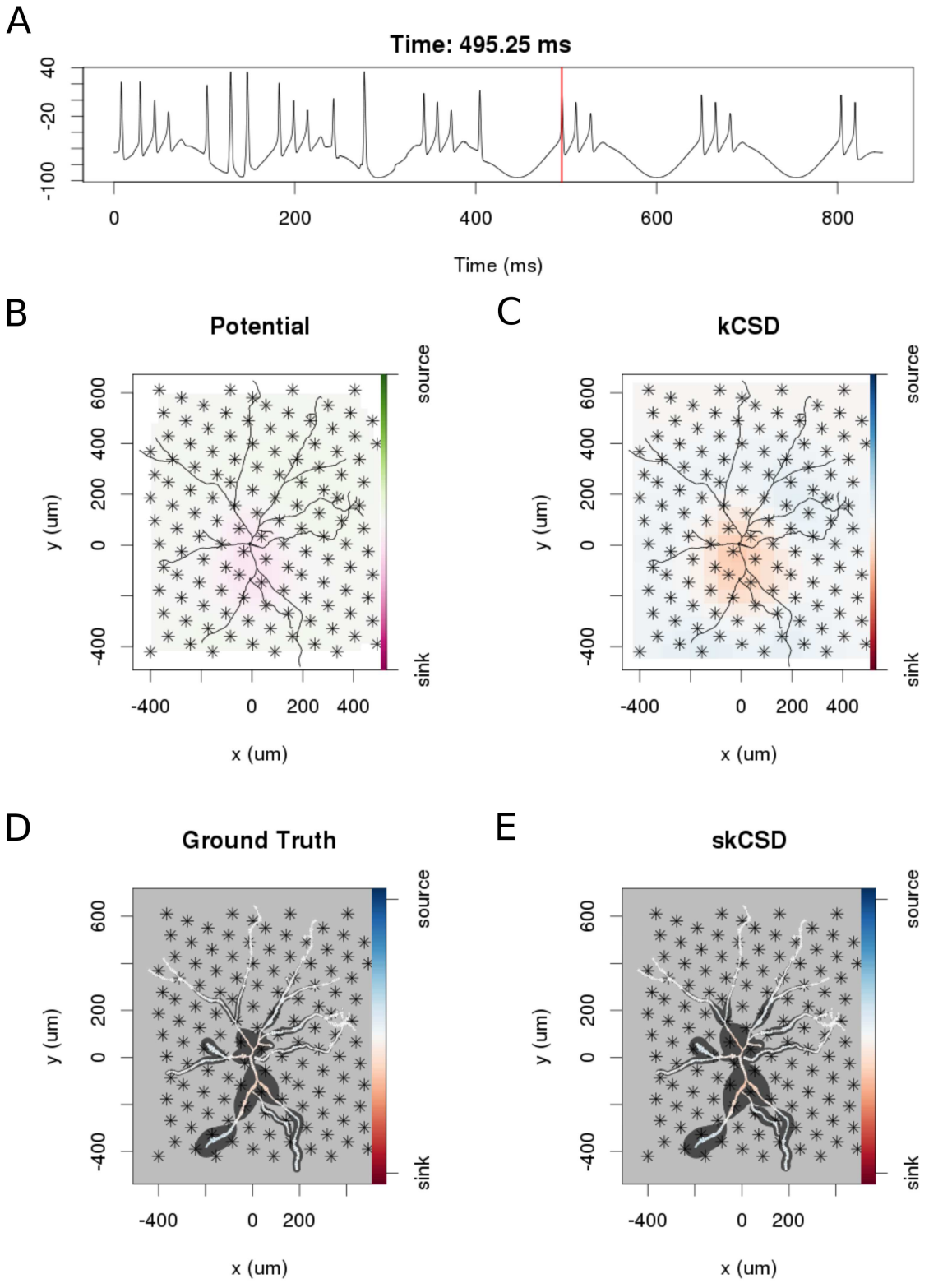

Figure 4.15: ***skCSD reconstruction of dendritic back-propagation patterns for a retinal ganglion cell model driven with oscillatory current.*** *Description on the next page.*

Figure 4.15: ***skCSD reconstruction of dendritic back-propagation patterns for a retinal ganglion cell model driven with oscillatory current.*** ***A*** *Somatic membrane potential during the simulation. The red line marks the time instant for which the remaining plots were made.* ***B*** *Extracellular potential interpolated between the simulated measurements computed at the electrodes, which are marked with asterisks.* ***C*** *kCSD reconstruction computed from the simulated measurements of the potential.* ***D*** *Spatial smoothing with a Gaussian kernel was applied to the ground truth membrane current to facilitate comparison with the skCSD reconstruction with the same spatial resolution level.* ***E*** *skCSD reconstruction computed from the simulated measurements of the potential.*

4.3.2.4 Dependence of reconstruction on noise level

So far we have assumed that the data are noise-free which is never true in an experiment. Both the measurement device and the neural tissue are potential sources of distorted data. To investigate how the performance of the method is influenced by noise, we added Gaussian white noise of differing amplitudes to the simulated extracellular recordings of Y-shaped cell described above. Fig. 4.16. A shows the smoothed ground truth we used. The Y-shaped neuron is placed on top of a MEA with a regular grid of 4x8 electrodes marked by asterisks. Fig. 4.16.B shows the noise-free reconstruction. Panel C–F of the figure show the reconstruction results for increasing measurement noise with signal to noise ratio, SNR$= 16, 4, 1$. The signal-to-noise ratio (SNR) here is the standard deviation of the simulated extracellular potentials normalized with the std of the added noise. The degradation of reconstruction visible on panels B anD to F is summarized in Fig. 4.16.C. As can be seen in the reconstruction plots (Fig. 4.16.D–F), the increasing noise actually does not seem to significantly alter the obtained reconstructions so the regularization is providing adequate correction, except for the noise on the order of signal (Fig. 4.16.F).

DOI:10.14753/SE.2020.2264

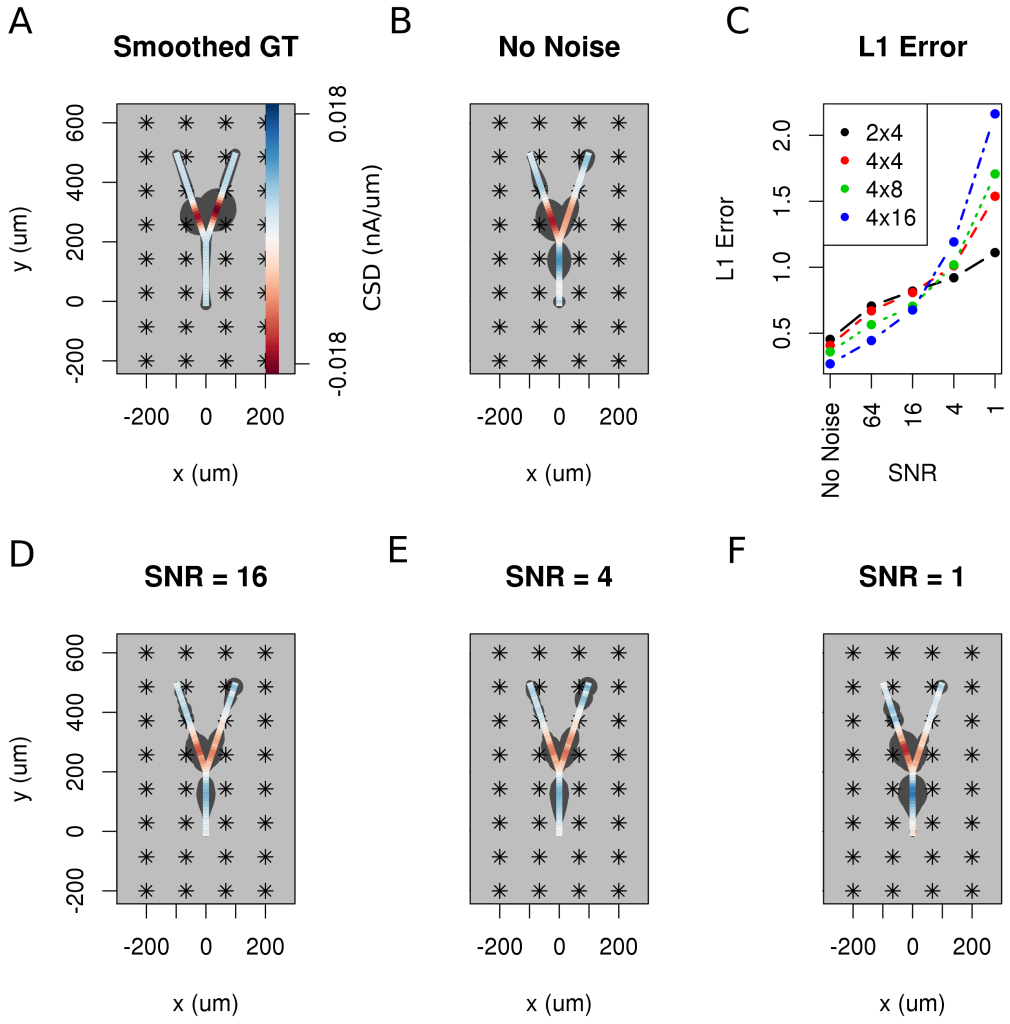

Figure 4.16: ***The effect of noise on the reconstruction.*** *The corrupting influence of noise on the skCSD reconstruction is shown with the example of simultaneous excitation of both branches of the Y-shaped cell close to the branching point in case of the 4x8 electrodes setup.* ***A*** *Smoothed ground truth CSD shown on the branching morphology used.* ***B,D,E,F*** *skCSD reconstructions in cases of no added noise and signal-to-noise ratio equal to 16, 4, 1, respectively. Even the highest noise considered does not fully disrupt the reconstructed source distribution, although increasing the noise systematically degrades the result. This is shown in* ***C****, where the L1 norm error of the reconstruction was calculated for the full length of the simulations. This is consistent for different electrode setups which are marked with various colors. While the setups consisting of more electrodes perform better for low noise, the reconstruction seems to be more sensitive to noise in these cases. This might be a side effect of a specific definition of error.*

4.3.2.5 Dependence of reconstruction on the number and arrangement of Recording Electrodes

Reconstruction of the distribution of the current sources along the morphology with skCSD (just like the reconstructions of smooth population distributions with kCSD) formally can be attempted from an arbitrary set of recordings, even a single electrode. While we do not expect enlightening results at this extreme, it is natural to ask the following questions: 1) to what extent can we trust the reconstruction in a given case, 2) which of the reconstructed features are real and which are artifacts of the method, and 3) how can the optimal parameters be selected for this method. We will return to these issues in the Discussion. Here we wish to investigate how the number of electrodes, the density of the grid, and the area covered by the MEA, affect the results.

To answer these questions, we selected a snapshot of simulation of the model of the ganglion cell with the specific membrane current distribution shown in Fig. 4.17.A. In Fig. 4.17.B–H we show 7 different reconstructions assuming different experimental setups, with differing numbers of electrodes, covering different area.

DOI:10.14753/SE.2020.2264

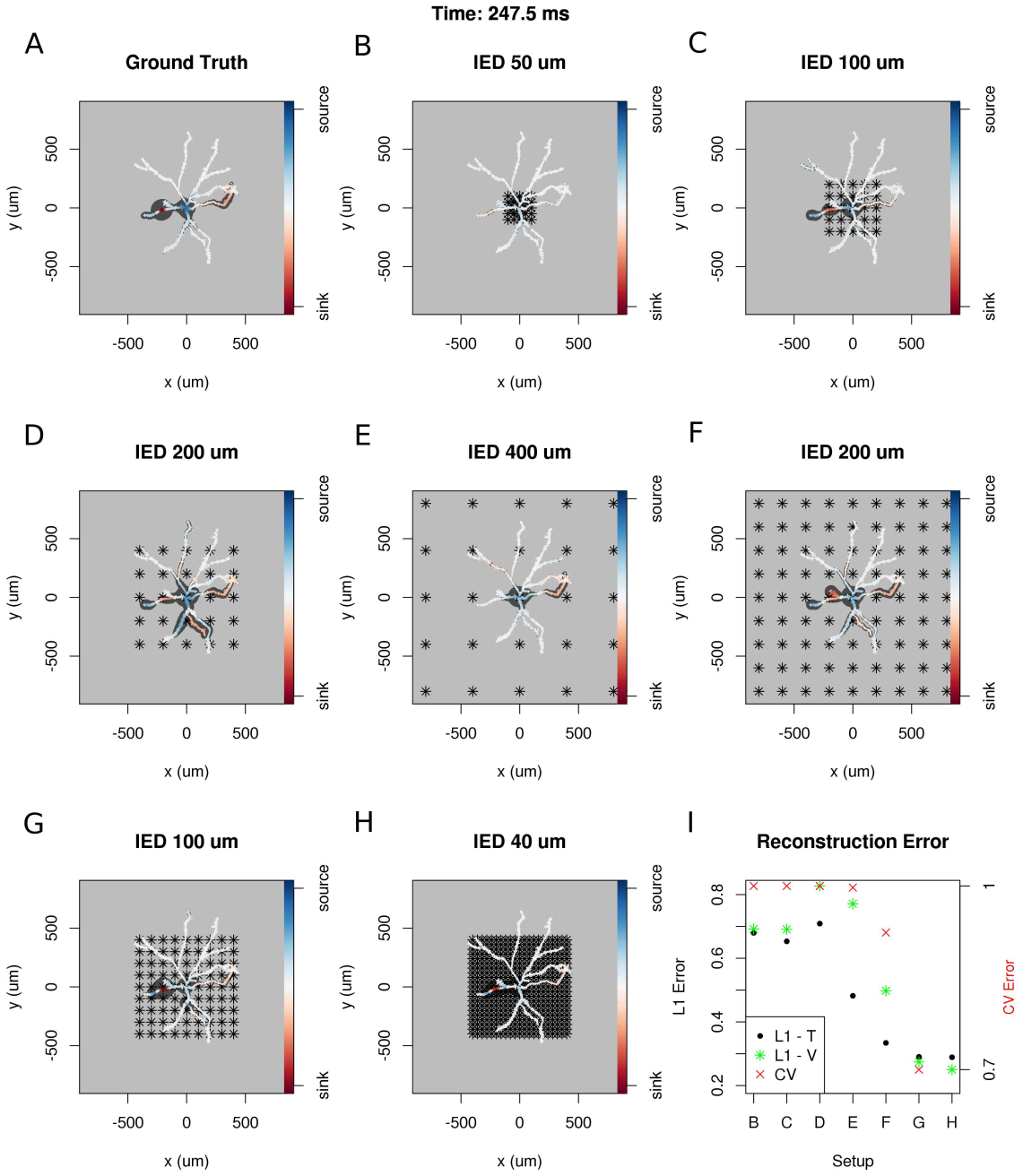

Figure 4.17: ***Dependence of skCSD reconstruction on multielectrode setup.*** *Description on the next page.*

DOI:10.14753/SE.2020.2264

Figure 4.17: ***Dependence of skCSD reconstruction on the multielectrode setup.*** *Figures A–H show morphology used in the simulation together with the distribution of current sources in branching morphology representation taken at 247.5 ms of the simulation. Figures B–H show additionally the electrode setup assumed.* ***A****. Smoothed ground truth CSD.* ***B****. Reconstructed sources for a setup of 5x5 electrodes with 50 µm interelectrode distance (IED) covering a small part of the cell morphology around the soma.* ***C****. Reconstructed sources for a setup of 5x5 electrodes with 100 µm IED covering a substantial part of the dendritic tree, which improves the reconstruction of the synaptic input on the left.* ***D****. Reconstructed sources for 5x5 setup with 200 µm IED setup; both sinks in the membrane currents are visible.* ***E****. Expanding the 5x5 electrode setup to 400 µm IED leads to a small number of electrodes placed in the vicinity of the cell which leads to a poor reconstruction.* ***F****. Increasing the number of electrodes to 9x9 while keeping the coverage, which leads to 200 µm IED, improves the reconstruction.* ***G****. Reducing IED in the previous example to 100 µm, which reduces the coverage of the MEA to the whole cell (same area as in panel* ***D****) bringing majority of the electrodes close to one of the dendrites, leads to one of the most faithful reconstructions among the ones shown in this figure.* ***H****. Shows results for a matrix of 21x21 contacts with 40 µm IED, covering the same area as in examples* ***D*** *and* ***G****. The results are very good but the improvement in reconstruction does not justify the use of so many contacts with so high density.* ***I****. Comparison of reconstruction errors for all the cases shown. Left axis: L1 norm error for the training (L1-T) and validation (L1-V) part . Right axis: leave-one-out cross-validation error (CV). The L1-T error is marked with black points, L1-V error is represented by green stars. Generally, the L1-V errors are a bit higher than the L1-T errors but show a similar tendency. Also the CV errors, which are drawn with red crosses, show a similar tendency. The reconstructions in panels* ***B–H*** *are for parameters determined with the L1-T error.*

DOI:10.14753/SE.2020.2264

In each case we selected the width of basis functions and the regularization parameter for the method by minimizing the L1 norm error calculated for the first 1000 time steps of the simulation or leave-one-out cross-validation error (L1-T and CV in Fig. 4.17.I). To verify the quality of reconstruction we computed the L1 norm error between the ground truth and reconstruction for the remaining 5800 time steps of the simulation. We found that minimization of L1 error gave better results and L1-V in Fig. 4.17.I shows the results for this case, however, the results obtained with minimization of CV error were often not much worse (not shown).

Given that L1 norm error can only be used where the ground truth is known, which is in simulations, we propose the following. Given the data necessary for application of the skCSD method, (neuronal morphology, positions of electrode contacts, and recorded signals) different CSD distributions should be assumed for the obtained morphology, reconstructions obtained for a range of parameters, then the L1 norm error could be used for optimization. Note that it is not necessary to actually simulate a model of the cell with proper membrane biophysics, which often is not known, although it might lead to more physiological test sources. It is sufficient to distribute the different sources along the morphology without making any assumptions concerning the biophysical properties of the neuronal membrane.

Once the parameters are obtained with this procedure, perform the analysis of actual experimental data with the obtained parameters. Performing the simulations and comparing the best reconstructions with the assumed ground truth has the further benefit of building intuition about which features of the real CSD survive in the reconstruction and which are distorted. This is another example of model-based data analysis which we believe becomes inevitable with the growing complexity of experimental paradigms, such as the one considered here.

We feel that the above procedure is optimal, since it not only gives optimal parameters, but also allows one to investigate which features are recovered and which are misformed. However, if only parameters for estimation are needed, CV error could be used, which is simpler and the results are often comparable.

The results obtained in this study are consistent with our expectations: the quality of reconstruction improves with the coverage of the morphology by the electrodes, with increasing density of probing, and with increasing number of probes (Fig. 4.17.I). Interestingly, it seems, that it is difficult to improve the reconstruction beyond a certain level, in consequence, the setups with moderate densities (on the order of 200 μm IED) can easily compete with setups at the edge of current developments (40 μm IED, Berdondini et al. 2005). We believe this is not a hard limit and that better results can be obtained here. This, however, requires further development of the methods.

4.3.2.6 Proof of Concept experiment: Spatial Current Source Distribution of Spike-triggered Averages

To examine the experimental feasibility of the skCSD method we analyzed data from a patch clamp electrode and a linear probe with 14 working electrodes recording signals simultaneously from a hippocampal pyramidal cell in an in vitro slice preparation (see Methods). As there is no ground truth data available in this case, the optimal width of the basis functions and the regularization parameter were selected using the L1 norm error and simulated data. To do this, we used the same simulation protocol as for the ganglion cell model. A snapshot of the reconstruction is shown in Fig. 4.18 at the moment of firing. In the resonstruction 0.05 ms before the spike the brief appearance of a sink (red) in the basal dendrites is visible which can be a consequence of the activation of voltage sensitive channels in the axon hillock, or the first axonal segment leading to the firing of the cell. Since there were no electrodes close to the axon initial segment, the skCSD method did not resolve it, instead it resolved to introduce the activity into the basal dendrite. This phenomenon is quickly replaced by a sink at the soma and in the proximal part of the apical dendritic tree, accompanied by sources (blue) in the basal and in the more distal apical dendrites. The extracellular potential on the second electrode reaches its minimum at 0.45 ms, which signals the peak of the spike. The deep red of the soma at this point signifies a strong sink, while the blue of the surrounding parts of the proximal apical and basal dendrites indicate the current sources set by the return currents. At 1.30 ms a source appears at the soma region, which indicates hyperpolarizing currents. Overall, the observed spatio-temporal CSD dynamics is dominated mostly by the somatic currents, responsible for the spike generation, and the corresponding counter currents. This example demonstrates the experimental feasibility of the skCSD method and may help in planning further experiments, aiming to reveal the spatial distribution and temporal dynamics of the synaptic input currents which evoke the firing of the neuron.

DOI:10.14753/SE.2020.2264

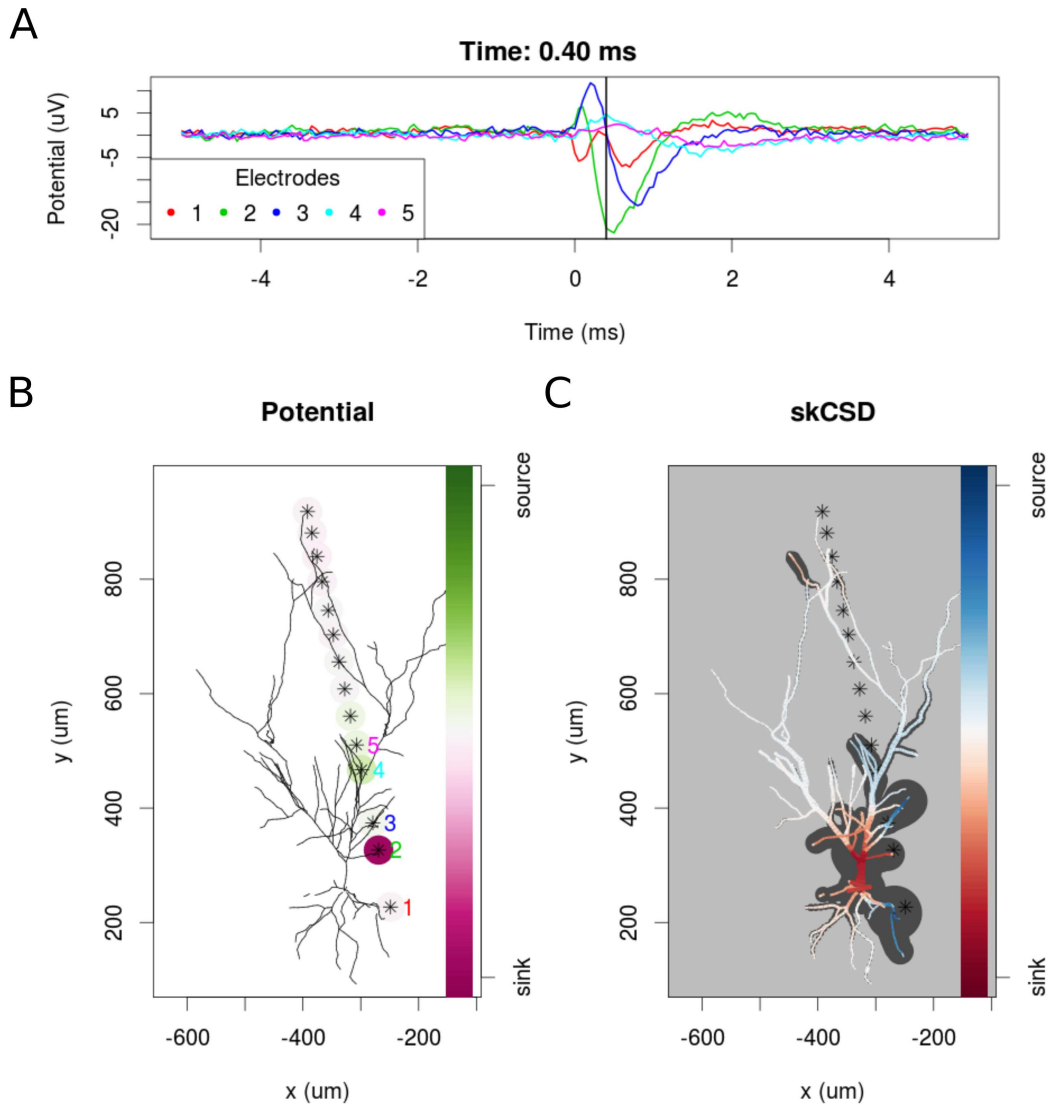

Figure 4.18: ***skCSD reconstruction of spike-triggered average for a hippocampal pyramidal cell A*** *Extracellular potentials measured with the 5 electrodes closest to the soma. The 0s marks the time of the membrane potential crossing the 0 mV threshold. The black vertical line marks the 0.40 ms time instant for which the extracellular potentials and skCSD reconstruction are shown.* ***B*** *Two-dimensional projection of the cell morphology and extracellular electrodes' positions marked by stars, the five electrodes used in the top panel of the figure are labeled with matching colors. The amplitudes of the measured potentials are shown as color-coded circles around the electrodes.* ***C*** *The skCSD reconstruction on the branching morphology representation. This is a snapshot of the cell firing, the red color indicates the sinks close to the soma, the blue marks the current sources on the dendrites.*

DOI:10.14753/SE.2020.2264

5 Discussion

5.1 Appearance of monopole current sources

In the field of neurophysiology, the shocking experimental result of the recent years was the non-zero monopole values measured and calculated [Riera et al. 2012]. This shattered the solid belief in the quasistatic approximation for single neurons. Although this view was challenged recently [Gratiy et al. 2017], we considered an other issue effecting the precision of reconstructions.

In our simulations we considered a simple and more complex neuron morphology with membrane currents summing up to zero. From the recordings of the virtual electrode grids of various interelectrode distances the tCSD and vCSD values were estimated and the monopole, dipole, quadrupole moments calculated. For both methods there was a nonzero monopole moment, the bigger the less numerous and further the electrodes were.

It is trivial, that the number of the recording electrodes limit the quality of reconstruction relying on that. The other side of having a certain number of electrode is, that this means finite sampling in space. As the tCSD method, which uses the finite difference method for solving the Poisson equation, the error of the estimation grows with the square of the grid constant [*Iterative Methods for Sparse Linear Systems*], which in this case is the interelectrode distance. The vCSD method uses more complex mathematical formulas, it is not so straightforward to give an estimation to the error. Nevertheless as it also involves the calculation of inverse matrices, one needs to pay attention to the numerical stability. Regardless of these, when applying this method, we assumed that the medium is homogeneous and isotropic, which was true in our simulation, but not fully in reality.

5.2 Effect of the not parallel cell-electrode positioning in the sCSD maps.

The theoretical methods rely on multiple assumptions due to the lack of information or to the complexity. Besides taking the quasistatic approximation of Maxwell's equations and modeling the extracellular field as a homogeneous and isotropic medium, the sCSD method has more specific, strict assumptions. The core idea of the sCSD is to model the cell as N point sources along a line. This is required by the constraints on the available information about the cell morphology and the theoretical framework. An other assumption is, that the axis of the cell is parallel to the linear probe. There is a real risk in experiments for this to

not to happen, which led to further investigation of this case. In simple simulations the axis of the cell was systematically tilted and the performance of the method analyzed.

Furthermore, it is difficult to compare the performance with other methods, as those are developed for different experimental setups and for calculating the CSD pattern for a population of neurons. When comparing to the tCSD method, which clearly was not developed for estimating the CSD distribution of single cells, we found that in the majority of the cases the sCSD method performed better, even if the assumption related to the parallelity of the cell and electrode was broken.

The significance of not positioning the electrode has to be understood also in the framework of the researcher using this method. Certainly, this method is able to show current source density maps about back-propagating signals on dendrites distinguishing only between apical and basal ones, and it is not able to show complex input patterns on the dendritic tree. There might be a small change in the values of the sCSD map due to a tilted electrode, but won't change the outcome dramatically.

5.3 skCSD

Observe that skCSD, like any other data analysis method, is not a magic wand. Technically, it can be applied to data coming from a single electrode just like the age profile of a human population can be estimated from a single specimen. Obviously, in both cases, the estimate would be a poor reflection of the distribution of interest. As we improve the sampling, the quality of the estimate improves, yet, ultimately, it is hard to judge a priori how many electrodes is enough and if our results obtain the required level of precision. We see two approaches to address this type of questions. One is through simulations, as we discussed. The other is analysis of the singular vectors arising in the decomposition of the matrix translating the measured potentials into the estimated CSD [*Discrete Inverse Problems*], however the necessary tools for kCSD and skCSD are still under development. We plan to investigate this further in the future.

Having obtained the distribution of currents it would be interesting to decompose it into physiologically meaningful components, such as synaptic currents, leak currents, voltage-gated currents for different channels, etc. This seems rather challenging and we do not see a direct way of achieving this from experimental data. It is possible that an application of statistical decomposition methods will prove useful, as in the case of kCSD for population activity [Łeski et al. 2009; Głabska et al. 2014]. However, we find the contributions to the extracellular potential from individual currents highly counter-intuitive [Głabska et al. 2016a].

Experimental Recommendations To attempt experimental application of skCSD we must have 1) an identified cell of known morphology, and 2) a set of simultaneous extracellular recordings of electric potential generated by this cell. Each aspect poses its challenges, some of which have been addressed here. Once we have the necessary data the natural question is how to select the parameters of the method in the specific context of a given setup, specific morphology, and recordings. Our investigations above give some indications. First, the electrodes selected for analysis should essentially uniformly cover the area spanned by the cell. This is illustrated in Fig. 4.13, which shows that some degree of irregularity does not significantly affect the reconstruction. Secondly, the basis should be selected so that the basis sources could resolve the features on the membrane we are interested in (narrow basis functions) with sufficient multiplicity, that smooth coverage of the cell can be ensured (see Fig. 4.14).

Clearly, as the irregularity of the setup grows we expect growing reconstruction errors. This can be studied with singular vectors of the operator transforming potential measurements into reconstructed sources, eq. 4.10, as discussed e.g. by [*Discrete Inverse Problems*]. We are convinced, however, that the most efficient approach to investigate the effects of these different parameters is through simulations. This is a natural place to apply the *model-based validation of data analysis* [Denker et al. 2014]. Our suggestion is to build a computational model of the cell. We believe that for the purpose of parameter selection assuming passive membrane in the dendrites should be sufficient, but of course, more realistic biophysical information may be included, especially if available. The model cell may be stimulated with synaptic input, with current injected, or even specific profiles of ground truth CSD may be placed along the cell. Then the extracellular potential must be computed at points where the actual electrodes are placed in the experiment. One can then investigate the effects of different parameter values on reconstruction and, for the analysis of actual experimental data, select those parameters minimizing prediction error on test data. The advantage of this procedure is two-fold. First, we end up with a selection of parameters adapted for the specific problem at hand. Secondly, we build intuition regarding the interpretation of the results for our specific cell and setup. This approach is the only way to address arbitrary electrode-cell configurations and to determine how much information we can extract in a given case.

We found that the best way to identify optimal parameters for reconstruction is by minimizing the L1 error between the reconstruction and the ground truth. Since we cannot have the ground truth in an experiment, but we can assume it in the model-based validation, this is another argument for the model-based validation approach. Obviously, to efficiently apply this technique the appropriate computational tools must be available.

Challenges of recording extracellular potentials and obtaining the morphology from the same cell Although, recording extracellular potential with a MEA, filling a neuron with a dye, and reconstructing its morphology, are standard experimental techniques, using them simultaneously remains a challenge due to the size of the experimental devices which need to be arranged within a small volume. Cells in the vicinity of the MEA can be filled individually by intracellular or juxtacellular electrodes, or with bulk dying. Individual recording and dying with a glass electrode provides not only the morphology, but also unambiguous spike times, giving an opportunity to determine the extracellular potential fingerprint of the recorded cell on the MEA. Although these would be favorable data, intracellular recording less than $100\mu m$ from the MEA is extremely challenging. Experimental setups featuring the necessary equipment already exist [Neto et al. 2016], but as far as we know, have not been used in this way. On the other hand, bulk dying techniques result in more filled neurons, although the quality of the dying, and thus the quality of the 3D morphology reconstructions, is considerably lower in these cases. Although there are methods for estimation of the cell position relative to the MEA [Somogyvári et al. 2005,Somogyvári et al. 2012], association of multiple optically labeled neurons with the recorded extracellular spike patterns is still unsolved.

Challenges of separating the activity of a single neuron from background We propose two experimental scenarios one could apply to separate the activity of the studied neuron from the background. If we can sort the spikes elicited by the neuron of interest we can calculate the spike-triggered averages of the potentials reducing all uncorrelated contributions. Unfortunately, in live tissue, contributions from neighboring cells will have some correlations due to shared inputs. Separation of the contribution of the neuron of interest from the correlated background can be obtained in two ways. One is decomposition of the activity into meaningful components, for example, as shown by [Somogyvári et al. 2015], the high amplitude correlated oscillatory background of hippocampal theta activity can be extracted with independent component analysis, allowing the determination of cell-type specific time course of the synaptic input. Alternatively one could consider combining skCSD with population kCSD analysis, i.e., consider basis sources covering the cell of interest as well as the space covering the whole population. This will be the subject of further study. The second experimental scenario to obtain the contributions to the extracellular potential from a specific cell is to drive the cell with intracellular current injection of known pattern, for example, with an oscillatory drive as we discussed (Fig. 4.15), and by averaging over multiple periods (event-based triggering). Again, further study is needed to establish the validity of this type of experimental procedure.

Challenges of using novel MEAs Handling data from high density MEAs with thousands of electrodes will require further studies, as the large numbers of small singular values of the kernel matrix may introduce numerical sensitivity to the reconstruction. Also, optimal selection of electrodes in case of programmable MEAs merits further investigations. We believe it is best to address such issues when actual experiments are attempted.

Importance of this work Traditional electrophysiology has focused on the electrical potential, which is relatively easy to access, from intracellular recordings, all kinds of patch clamp, juxtacellular, to extracellular and voltage sensitive dyes. While the relation of the actual measurement to the voltage at a point may significantly differ, often this is a reasonable interpretation, if needed, more realistic models of measurement can be considered, for example, averaging over the contact surface for extracellular electrodes, etc [Moulin et al. 2008; Torbjrn et al. 2016].

Already in the middle of the 20th century, Walter H. Pitts observed that for recordings obtained with regular grids one can approximate the Poisson equation to estimate the distribution of current sources in the tissue [Pitts 1952]. His approach assumed recordings on a regular 3D grid, which was challenging to obtain for some 60 years [Łeski et al. 2007]. However, with the work of Nicholson and Freeman [Nicholson et al. 1975] 1D CSD analysis became attractive, as summarized by Ulla Mitzdorf [Mitzdorf 1985]. In 2012 we proposed how to overcome the restriction of regular grids with a kernel approach which both allows to use arbitrary distribution of contacts and corrects for noise [Potworowski et al. 2012]. All the previous work, however, always assumed the contributions to the extracellular potential coming from the whole tissue and smooth in the estimation region.

In the present work we show for the first time how a collection of extracellular recordings in combination with a cell morphology can be used to estimate the current sources located on the cell contributing to the recorded potential. Since it is now feasible experimentally to obtain the relevant data, we believe that the method proposed here may find its uses to constrain the biophysical properties of the neuron membrane, facilitate verification of morphological reconstructions, as well as guide new discoveries by offering a more global picture of the distribution of the currents along the cell morphology, giving a coherent view of the global synaptic bombardment and return currents within a cell.

DOI:10.14753/SE.2020.2264

6 Conclusions

We proposed that the discrete spatio-temporal sampling of the extracellular potential and the approximations of the mathematical tools to calculate the current source density distribution causes the observation of monopoles. Simulation containing a 3D electrode grid recording the extracellular potentials of a spiking neuron was used as a tool to support our conclusion.

The sCSD method aims to estimate the CSD distribution on linear cell model. This novel method uses innovative assumptions about the experimental setup and even about the cell-electrode distance estimation for the current source density distribution.

To test the performance, we generated simulated, known data. It has the benefit of having full control of the parameters and knowing the values.

In this thesis we presented the study of cases, when a key assumption of the sCSD method are not satisfied. This is always a key point in theoretical approaches, as it can help to understand the experimental results and their validity. As shown in Figure 4.8, the sCSD performed well, it gave meaningful results with reasonable RMSE even when $= 20^{\circ}$. In experiments it is possible to reach more ideal setup when for example inserting the linear probe perpendicularly to the brain surface in mice and estimating the sCSD distribution of pyramidal neurons.

The developed skCSD method aims to estimate the current source density along the morphology of single neurons based on extracellular recordings and the morphology. For validation the usage of the method was shown on several simulational and also an experimental data. First, a simple setup of a ball-and-stick neuron model and a laminar probe was considered. We showed that introducing more electrodes to cover the same area leads to increased spatial resolution of the method allowing reconstruction of higher Fourier modes of the CSD generating the measured potentials (Fig. 4.10). In a dynamic scenario of multiple synaptic inputs impinging on the cell, higher density of probes leads to higher reconstruction precision allowing us to distinguish individual inputs (Fig. 4.11). Testing the reconstruction against the known CSD (the ground truth) shows a clear transition from poor to faithful reconstruction when the electrode distribution becomes dense enough to capture the fine detail of the CSD profile to be reconstructed (Fig. 4.10.E). We also applied this method to more complex neuron morphologies, namely the Y-shape and ganglion cell. Using the Y-shaped morphology we showed that i) synaptic inputs activating different dendrites can be separated, Fig. 4.12; ii) skCSD provides meaningful information about the membrane CSD in cases, when the interpolated LFP and standard, population CSD analyses, are not informative, Fig. 4.12; iii) the reconstruction is not sensitive to a specific selection of electrode placement, Fig. 4.13 and 4.16; and iv) even significant additive noise

DOI:10.14753/SE.2020.2264

(SNR=1) is not prohibitive for the reconstruction, Fig. 4.16. As expected, the reconstructed CSD profiles became more detailed with increasing electrode number over a fixed area (Fig. 4.13 and 4.17).

The MEAs differed in the inter-electrode distances for the simulated setups, as well as in the area they covered, ranging from an area close to the soma to roughly four times the size of the smallest square covering the whole morphology. The best results were obtained when we used the electrodes from the region which closely covered the cell; a reduction of inter-electrode distance from 100μm to 40μm yielded less impressive results than selecting the electrodes from the smallest square covering the convex hull span by the morphology. Our study, assumed realistic cell morphology of the ganglion cell and commercially available MEA designs, as well as realistic cell activity, showed that it is feasible to reconstruct the distribution of the current sources in realistic, noisy situations. Even in this case the method provided an adequate estimation for the experimental data, even though in this setup only the CSD distribution related to the spike-triggered average was considered.

DOI:10.14753/SE.2020.2264

7 Summary

In this work theoretical methods related to the estimation of the current source density distributions of single cells and results of their application were described. The quasistatic estimation is widely used in theoretical methods related to neurons, hence the appearance of monopole current sources in experiments contradicts it. Through examples we investigated the role of the limitations of the available experimental tools and the applied mathematical methods in the apparent monopole sources. In case of finite spatial sampling we cannot hope to reach perfect reconstruction, the discrete calculation of Laplacian operator induces error, which depends on the interelectrode distance.

Furthermore, a crucial point of each theoretical method is the investigation of not ideal scenarios, which are likely to happen in reality. We analyzed the change in the estimation of the sCSD method [Somogyvári et al. 2012], when the experimental setup is violating one of the main assumption: the cell is not completely parallel with the electrode. We built simulations to study the distortion: a range of angles and cell to electrode distances were considered and the sCSD estimations compared with the ground truth. We found that the sCSD method still performs better than the tCSD when the tilting is not too big, meaning that is experimentally easily achievable. Furthermore the distance estimation is only slightly influenced by realistic tilting as well.

Finally, in this work we introduced the skCSD method [Cserpán 2017] to estimate the distribution of current sources along the whole morphology of a neuron given its known morphology and a set of simultaneous extracellular recordings of potential generated predominantly by this cell. After the derivation of the method, simulated and experimental examples of application are shown. Assuming the ball-and-stick neuron model and a laminar probe parallel to the cell, we studied the basic viability of this method. We showed that introducing more electrodes leads to increased spatial resolution of the method allowing the reconstruction of higher Fourier modes of the CSD or or more detailed information about synaptic inputs generating the measured potentials.

With the Y-shaped and ganglion cell models in a setup with multi-electrode arrays of different designs, we could draw conclusions on the optimal experimental arrangements and verify the performance of the method.

The skCSD method performed adequately for the proof of concept experimental data, even if the nature of the experiment allowed only the reconstruction of the general features of the spatio-temporal current source density distribution patterns of the spike-triggered average.

DOI:10.14753/SE.2020.2264

8 Összefoglalás

Ezen munkában egyes idegsejtek áramforrássűrűség-eloszlásainak becslésére alkalmas módszereket, illetve ezek alkalmazásával kapcsolatos eredményeinket mutattuk be. Először az idegsejtekre alkalmazott módszerek kvázisztatikus közelítésének ellentmondó, a kísérletekben kimért monopól áramforrások megjelenésének magyarázatát tűztük ki célul. A rendelkezésre álló kísérleti és alkalmazott elméleti eszközök limitációit példákon keresztül vizsgáltuk. Véges térbeli mintavételezés esetén nem remélhető tökéletes rekonstrukció, a Laplace operátor diszkrét számolása is hibát vezet be, ami függ az elektródák közötti távolságtól.

Továbbá minden elméleti módszer kényes pontja a gyakorlatban előforduló, ám a feltételezéseknek nem megfelelő eset. Megvizsgáltuk az sCSD módszer [Somogyvári et al. 2012] becslésében bekövetkező változást, mikor a kísérleti elrendezés sérti az egyik fő feltételezést, azaz az idegsejt fő tengelye nem párhuzamos a lineáris elektródával. Az eltérés nyomonkövetésére szimulációkat készítettünk. Az sCSD módszer becslését egy adott szög-, és távolságtartományban összehasonlítottuk az eredeti eloszlással. Azt találtuk, hogy az sCSD módszer jobban teljesít, mint a tCSD, azon szögek esetén, amely pontosság kísérletekben is könnyen megvalósítható. Ezenkívül ilyen esetekben a távolságbecslés is még viszonylag pontos.

Végül bemutattunk az skCSD módszert [Cserpán 2017], mely az egyes idegsejtek teljes morfológiáján képes az áramforrássűrűség-eloszlásainak becslésére. Ehhez szükséges a morfológia ismerete illetve az ezen sejt működéséhez kapcsolódó extracelluláris potenciálmintázat. A módszer levezetése után, szimulált és kísérleti példákon keresztül mutattuk be az alkalmazhatóságát. A labda-rúd idegsejtmodell és lineáris próba elrendezés esetén a módszer alapvető tulajdonságait néztük. Megmutattuk, hogy több elektróda alkalmazása esetén jobb térbeli felbontás érhető el, a mért potenciálokat előállító magasabb CSD Fourier-módusok vagy részletesebb szinaptikus bemeneti mintázatok rekonstruálhatók.

Az Y- és ganglion-modellek és különféle multielekróda-rendszerekből álló elrendezés esetén az optimális elrendezésre és a módszer teljesítményét illetően vontunk le további következtetéseket.

Az skCSD módszer megfelelően teljesített a kísérleti adat esetén is, még ha az csak a sejt tüzelésre átlagolt tér-időbeli áramforrássűrűség-eloszlás mintázatok becslését jelentette is.

DOI:10.14753/SE.2020.2264

9 Bibliography

Ascoli, Giorgio A. (2006). “Mobilizing the base of neuroscience data: The case of neuronal morphologies”. eng. In: Nat Rev Neurosci 7.4, pp. 318–324.

Bakkum, Douglas J., Urs Frey, Milos Radivojevic, Thomas L. Russell, Jan Müller, Michele Fiscella, Hirokazu Takahashi, and Andreas Hierlemann (2013). “Tracking axonal action potential propagation on a high-density microelectrode array across hundreds of sites”. eng. In: Nat Commun 4.1, p. 2181.

Berdondini Luca, P. D. Van Der Wal Olivier Guenat Nicolaas F. de Rooij Milena Koudelka-Hep P. Seitz R. Kaufmann P. Metzler N. Blanc and S. Rohr (2005). “High-density electrode array for imaging in vitro electrophysiological activity”. eng. In: Biosens. Bioelectron. 21.1, pp. 167–174.

Buzsáki, György (2004). “Large-scale recording of neuronal ensembles”. In: Nat Neurosci 7.5, pp. 446–451.

Buzsáki, György, Costas A. Anastassiou, and Christof Koch (2012). “The origin of extracellular fields and currents — EEG, ECoG, LFP and spikes”. In: Nat Rev Neurosci 13.6, pp. 407–420.

Cabo, Alejandro and Jorge J Riera (2014). “How the active and diffusional nature of brain tissues can generate monopole signals at micrometer sized measures”. In: arXiv preprint arXiv:1410.0274.

Cannon, R.C, D.A Turner, G.K Pyapali, and H.V Wheal (1998). “An on-line archive of reconstructed hippocampal neurons”. In: J. Neurosci. Methods 84.1-2, pp. 49–54.

Chichilnisky, E.J. (2001). “A simple white noise analysis of neuronal light responses”. In: Network: Computation in Neural Systems 12.2, pp. 199–213.

Cserpán, Dorottya (2017). *Single cell kernel Current Source Density*. Github. https://github.com/csdori/skCSD.301edcb.

Denker, Michael, Gaute Einevoll, Felix Franke, Sonja Grün, Espen Hagen, Jason Kerr, Martin Nawrot, Torbjørn Bækø Ness, Raphael Ritz, Leslie Smith, Thomas Wachtler, and Daniel Wójcik (2014). *Report from the 1st INCF Workshop on Validation of Analysis Methods*. Tech. rep. INCF.

Einevoll, Gaute, Henrik Lindén, Tom Tetzlaff, Szymon ski, and Klas Pettersen. “Local field potential: Biophysical origin and analysis. Biophysical Origin and Analysis”. In: *Principles of Neural Coding*. Ed. by R. Quian Quiroga and S. Panzeri. CRC Press, Boca Raton (2013). Chap. Local Field Potentials, pp. 37–60.

Einevoll, Gaute T., Christoph Kayser, Nikos K. Logothetis, and Stefano Panzeri (2013). “Modelling and analysis of local field potentials for studying the function of cortical circuits”. In: Nat Rev Neurosci 14.11, pp. 770–785.

Ferrea, Enrico, Alessandro Maccione, Lucian Medrihan, Thierry Nieus, Diego Ghezzi, Pietro Baldelli, Fabio Benfenati, and Luca Berdondini (2012). “Large-scale, high-resolution electrophysiological imaging of field potentials in brain slices with micro-electronic multielectrode arrays”. eng. In: Front. Neural Circuits 6, p. 80.

Frey, U., U. Egert, F. Heer, S. Hafizovic, and A. Hierlemann (2009). “Microelectronic system for high-resolution mapping of extracellular electric fields applied to brain slices”. eng. In: Biosens. Bioelectron. 24.7, pp. 2191–2198.

Gold, Carl, Darrell A. Henze, Christof Koch, and György Buzsáki (2006). “On the Origin of the Extracellular Action Potential Waveform: A Modeling Study”. In: J. Neurophysiol. 95.5 (5), pp. 3113–3128.

Gratiy, Sergey L., Klas H. Pettersen, Gaute T. Einevoll, and Anders M. Dale (2013). “Pitfalls in the interpretation of multielectrode data: On the infeasibility of the neuronal current-source monopoles”. In: J. Neurophysiol. 109.6, pp. 1681–1682.

Gratiy, Sergey L., Geir Halnes, Daniel Denman, Michael J. Hawrylycz, Christof Koch, Gaute T. Einevoll, and Costas A. Anastassiou (2017). “From Maxwell’s equations to the theory of current-source density analysis”. In: Eur J Neurosci 45.8, pp. 1013–1023.

Gross, Charles G. (2002). “Genealogy of the “Grandmother Cell””. In: Neuroscientist 8.5, pp. 512–518.

Głabska, Helena, Jan Potworowski, Szymon Łeski, and Daniel K. Wójcik (2014). “Independent Components of Neural Activity Carry Information on Individual Populations”. eng. In: PLoS ONE 9.8, e105071.

Głabska, Helena, Chaitanya Chintaluri, and Daniel K. Wójcik (2016a). “Collection of Simulated Data from a Thalamocortical Network Model”. In: Neuroinform 15.1 (1), pp. 87–99.

Głabska, Helena T., Eivind Norheim, Anna Devor, Anders M. Dale, Gaute T. Einevoll, and Daniel K. Wójcik (2016b). “Generalized Laminar Population Analysis (gLPA) for Interpretation of Multielectrode Data from Cortex”. eng. In: Front. Neuroinform. 10, p. 1.

Hafting, Torkel, Marianne Fyhn, Sturla Molden, May-Britt Moser, and Edvard I. Moser (2005). “Microstructure of a spatial map in the entorhinal cortex”. In: Nature 436.7052, pp. 801–806.

Hansen, Per Christian. *Discrete Inverse Problems. Insight and Algorithms*. Society for Industrial and Applied Mathematics, Philadelphia (2010), pp. 15–90.

Henze, Darrell A., Zsolt Borhegyi, Jozsef Csicsvari, Akira Mamiya, Kenneth D. Harris, and György Buzsáki (2000). “Intracellular Features Predicted by Extracellular Recordings in the Hippocampus In Vivo”. In: J. Neurophysiol. 84.1 (1), pp. 390–400.

Hottowy, Paweł, Andrzej Skoczeń, Deborah E Gunning, Sergei Kachiguine, Keith Mathieson, Alexander Sher, Piotr Wiacek, Alan M Litke, and Władysław Dabrowski (2012). "Properties and application of a multichannel integrated circuit for low-artifact, patterned electrical stimulation of neural tissue". In: J. Neural Eng. 9.6, p. 066005.

Ishizuka, Norio, W. Maxwell Cowan, and David G. Amaral (1995). "A quantitative analysis of the dendritic organization of pyramidal cells in the rat hippocampus". In: J. Comp. Neurol. 362.1, pp. 17–45.

Jäckel, David, Douglas J. Bakkum, Thomas L. Russell, Jan Müller, Milos Radivojevic, Urs Frey, Felix Franke, and Andreas Hierlemann (2017). "Combination of High-density Microelectrode Array and Patch Clamp Recordings to Enable Studies of Multisynaptic Integration". In: Sci Rep 7.1 (1), p. 978.

Kerekes, Bálint Péter, Kinga Tóth, Attila Kaszás, Balázs Chiovini, Zoltán Szadai, Gergely Szalay, Dénes Pálfi, Attila Bagó, Klaudia Spitzer, Balázs Rózsa, István Ulbert, and Lucia Wittner (2014). "Combined two-photon imaging, electrophysiological, and anatomical investigation of the human neocortexin vitro". In: Neurophoton 1.1, p. 011013.

Kong, Jee-Hyun, Daniel R. Fish, Rebecca L. Rockhill, and Richard H. Masland (2005). "Diversity of ganglion cells in the mouse retina: Unsupervised morphological classification and its limits". eng. In: J. Comp. Neurol. 489.3, pp. 293–310.

Kwan, Mei-Ko (1962). "Graphic programming using odd or even points". In: Chinese Math 1.273-277, p. 110.

Lewandowska, Marta K., Miloš Radivojević, David Jäckel, Jan Müller, and Andreas R. Hierlemann (2016). "Cortical Axons, Isolated in Channels, Display Activity-Dependent Signal Modulation as a Result of Targeted Stimulation". eng. In: Front. Neurosci. 10, p. 83.

Lindén, Henrik, Klas H. Pettersen, and Gaute T. Einevoll (2010). "Intrinsic dendritic filtering gives low-pass power spectra of local field potentials". In: J Comput Neurosci 29.3 (3), pp. 423–444.

Lindén, Henrik, Espen Hagen, Szymon Łeski, Eivind S. Norheim, Klas H. Pettersen, and Gaute T. Einevoll (2014). "LFPy: A tool for biophysical simulation of extracellular potentials generated by detailed model neurons". eng. In: Front. Neuroinform. 7, p. 41.

Mechler, Ferenc and Jonathan D. Victor (2011a). "Dipole characterization of single neurons from their extracellular action potentials". eng. In: J Comput Neurosci 32.1, pp. 73–100.

Mechler, Ferenc, Jonathan D. Victor, Ifije Ohiorhenuan, Anita M. Schmid, and Qin Hu (2011b). "Three-dimensional localization of neurons in cortical tetrode recordings". eng. In: J. Neurophysiol. 106.2, pp. 828–848.

Mikulovic, Sanja, Carlos Ernesto Restrepo, Samer Siwani, Pavol Bauer, Stefano Pupe, Adriano B. L. Tort, Klas Kullander, and Richardson N. Leão (2018). "Ventral hippocampal OLM cells control type 2 theta oscillations and response to predator odor". In: Nat Commun 9.1, p. 3638.

Mitzdorf, Ulla (1985). "Current source-density method and application in cat cerebral cortex: Investigation of evoked potentials and EEG phenomena". In: Physiol. Rev. 65.1, pp. 37–100.

Moulin, Céline, Alain Glière, Daniel Barbier, Sebastien Joucla, Blaise Yvert, Pascal Mailley, and Régis Guillemaud (2008). "A New 3-D Finite-Element Model Based on Thin-Film Approximation for Microelectrode Array Recording of Extracellular Action Potential". In: IEEE Trans. Biomed. Eng. 55.2, pp. 683–692.

Muthmann, Jens-Oliver, Hayder Amin, Evelyne Sernagor, Alessandro Maccione, Dagmara Panas, Luca Berdondini, Upinder S. Bhalla, and Matthias H. Hennig (2015). "Spike Detection for Large Neural Populations Using High Density Multielectrode Arrays". eng. In: Front. Neuroinform. 9, p. 28.

Neher, Erwin and Bert Sakmann (1976). "Single-channel currents recorded from membrane of denervated frog muscle fibres". eng. In: Nature 260.5554, pp. 799–802.

Neto, Joana P., Gonçalo Lopes, João Frazão, Joana Nogueira, Pedro Lacerda, Pedro Baião, Arno Aarts, Alexandru Andrei, Silke Musa, Elvira Fortunato, Pedro Barquinha, and Adam R. Kampff (2016). "Validating silicon polytrodes with paired juxtacellular recordings: Method and dataset". In: J. Neurophysiol. 116.2, pp. 892–903.

Nicholson, C. and J. A. Freeman (1975). "Theory of current source-density analysis and determination of conductivity tensor for anuran cerebellum". In: J. Neurophysiol. 38.2, pp. 356–368.

Nyquist, Harry (1928). "Certain topics in telegraph transmission theory". In: Transactions of the American Institute of Electrical Engineers 47.2, pp. 617–644.

Obien, Marie Engelene J., Kosmas Deligkaris, Torsten Bullmann, Douglas J. Bakkum, and Urs Frey (2015). "Revealing neuronal function through microelectrode array recordings". eng. In: Front. Neurosci. 8, p. 423.

O'Keefe, John and Jonathan Dostrovsky (1971). "The hippocampus as a spatial map: Preliminary evidence from unit activity in the freely-moving rat." In: Brain research.

O'Keefe, John and Neil Burgess (1996). "Geometric determinants of the place fields of hippocampal neurons". In: Nature 381.6581, pp. 425–428.

Pettersen, Klas H., Anna Devor, Istvan Ulbert, Anders M. Dale, and Gaute T. Einevoll (2006). "Current-source density estimation based on inversion of electrostatic forward solution: Effects of finite extent of neuronal activity and conductivity discontinuities". In: J. Neurosci. Methods 154.1-2, pp. 116–133.

Pitts, Walter (1952). “Investigations on synaptic transmission”. In: *Cybernetics, Trans. 9th Conf. Josiah Macy Foundation H. von Foerster*. New York, pp. 159–166.

Potworowski, Jan, Wit Jakuczun, Szymon Łski, and Daniel Wójcik (2012). “Kernel Current Source Density Method”. eng. In: Neural Comput. 24.2, pp. 541–575.

Quiroga, R Quian, Leila Reddy, Gabriel Kreiman, Christof Koch, and Itzhak Fried (2005). “Invariant visual representation by single neurons in the human brain”. In: Nature 435.7045, pp. 1102–1107.

Rey, Hernan Gonzalo, Carlos Pedreira, and Rodrigo Quian Quiroga (2015). “Past, present and future of spike sorting techniques”. In: Brain Res. Bull. 119, pp. 106–117.

Riera, Jorge and Alejandro Cabo (2013). “Reply to Gratiy et al.” In: J. Neurophysiol. 109.6. PMID: 23503558, pp. 1684–1685.

Riera, Jorge J., Takeshi Ogawa, Takakuni Goto, Akira Sumiyoshi, Hiroi Nonaka, Alan Evans, Hiroyoshi Miyakawa, and Ryuta Kawashima (2012). “Pitfalls in the dipolar model for the neocortical EEG sources”. In: J. Neurophysiol. 108.4, pp. 956–975.

Riera, Jorge J., Takakuni Goto, and Ryuta Kawashima (2014). “A methodology for fast assessments to the electrical activity of barrel fields in vivo: From population inputs to single unit outputs”. In: Front. Neural Circuits 8, p. 4.

Rizzolatti, Giacomo and Laila Craighero (2004). “The Mirror-Neuron System”. In: Annu. Rev. Neurosci. 27.1, pp. 169–192.

Saad, Yousef. *Iterative Methods for Sparse Linear Systems*. Computer Science Series. Society for Industrial and Applied Mathematics,Philadelphia (2003), p. 51.

Somogyvári, Zoltán, Zsigmond Benkő, Józsi Z. Jálics, Lisa Roux, and Berényi Antal (2015). “Determination of spatio- temporal input current patterns of single hippocampal neurons based on extracellular potential measurements”. In: Program No. 267.02. Society for Neuroscience, 2015.

Somogyvári, Zoltán, László Zalányi, István Ulbert, and Péter Érdi (2005). “Model-based source localization of extracellular action potentials”. eng. In: J. Neurosci. Methods 147.2, pp. 126–137.

Somogyvári, Zoltán, Dorottya Cserpán, István Ulbert, and Péter Érdi (2012). “Localization of single-cell current sources based on extracellular potential patterns: The spike CSD method. Localization of single-cell current sources: the sCSD”. eng. In: Eur. J. Neurosci. 36.10, pp. 3299–3313.

Taube Jeffrey S., Robert U. Muller and James B. Ranck (1990). “Head-direction cells recorded from the postsubiculum in freely moving rats. I. Description and quantitative analysis”. In: Journal of Neuroscience 10.2, pp. 420–435.

Torbjrn, Ness, Chintaluri Chaitanya, Potworowski Jan, Leski Szymon, Glabska Helena, Wjcik Daniel, and Einevoll Gaute (2016). “Modelling And Analysis Of Electrical

Potentials Recorded In Microelectrode Arrays (MEAs)". In: Front. Neurosci. 10.4, pp. 403–426.

Wei, Dong-Sheng, Yan-Ai Mei, Ashish Bagal, Joseph PY Kao, Scott M Thompson, and Cha-Min Tang (2001). "Compartmentalized and binary behavior of terminal dendrites in hippocampal pyramidal neurons". In: Science 293.5538, pp. 2272–2275.

Wójcik, Daniel K. "Current Source Density (CSD) Analysis". In: *Encyclopedia of Computational Neuroscience*. Ed. by Dieter Jaeger and Ranu Jung. Springer, New York (2015).

Łeski, Szymon, Daniel K. Wójcik, Joanna Tereszczuk, Daniel A. Świejkowski, Ewa Kublik, and Andrzej Wróbel (2007). "Inverse Current-Source Density Method in 3D: Reconstruction Fidelity, Boundary Effects, and Influence of Distant Sources". In: Neuroinform 5.4, pp. 207–222.

Łeski, Szymon, Ewa Kublik, Daniel A. Świejkowski, Andrzej Wróbel, and Daniel K. Wójcik (2009). "Extracting functional components of neural dynamics with Independent Component Analysis and inverse Current Source Density". In: J Comput Neurosci 29.3 (3), pp. 459–473.

Łeski, Szymon, Klas H. Pettersen, Beth Tunstall, Gaute T. Einevoll, John Gigg, and Daniel K. Wójcik (2011). "Inverse Current Source Density Method in Two Dimensions: Inferring Neural Activation from Multielectrode Recordings". eng. In: Neuroinform 9.4, pp. 401–425.

DOI:10.14753/SE.2020.2264

10 Author's Publications

Related to the thesis

- Cserpan D, Meszena D, Wittner L, Toth K, Ulbert I, Somogyvari Z, Wojcik D: "Revealing the Distribution of Transmembrane Currents along the Dendritic Tree of a Neuron with Known Morphology from Extracellular Recordings" eLife 2017;6:e29384
- Somogyvari Z, Cserpan D, Ulbert I, Erdi P: "Localization of single cell current sources based on extracellular potentials patterns: the spike CSD method", European Journal of Neuroscience 36, Issue 1, November 2012.

Other publications

- Zatonyi A, Borhegyi Z, Srivastava M, Cserpan D, Somogyvari Z, Kisvárday Z, Fekete Z: "Functional brain mapping using optical imaging of intrinsic signals and simultaneous high-resolution cortical electrophysiology with a flexible, transparent microelectrode array", SENSORS AND ACTUATORS B-CHEMICAL 273: pp. 519-526. ,2018
- Zatonyi A, Borhegyi Z, Cserpan D, Somogyvari Z, Srivastava M, Kisvárday Z, Fekete Z: "Optical Imaging of Intrinsic Neural Signals and Simultaneous MicroECoG Recording Using Polyimide Implants", Proceedings of Eurosensors 2017, Paper 610. 4 p.,2017
- Kantor O, Cserpan D, Volgyi B, Lukats A, Somogyvari Z: " The Retinal TNAP. In: Fonta C., Negyessy L. (eds) Neuronal Tissue-Nonspecific Alkaline Phosphatase (TNAP)". Subcellular Biochemistry, vol 76. Springer, Dordrecht. 2015

DOI:10.14753/SE.2020.2264

11 Acknowledgement

In this section I would express my gratefulness to people, who helped me on my rocky way of finishing this work. My main guide, not only on a scientific path, but in many other field of life was Zoltán Somogyvári. He introduced me to the adventurous and uplifting world of being a researcher and is my hero. This thesis is only finished now as Péter Érdi kept me going on this track, furthermore he gave me many possibilities and big chances in terms of experiences and career. Thanks to him, I had the chance to visit Kalamazoo College for few months, and get to know the ”culture of science and teaching”. Daniel Wójcik has an utmost importance in my carrier as he supervised and supported me during our work together. He granted me the opportunity to visit his Laboratory of Neuroinformatics at Nencki Institute of Experimental Biology, where I gained besides a lot of knowledge also great experiences. I am also grateful to his whole lab for the support and great atmosphere. He supervised in a very gentle, patient and supportive way. I was not alone on my way, other members of the team were always available in case of help needed. Special thanks to Zsigmond Benkő, my fellow in the office, who was always a partner in ups and downs in our daily life. I am indebted to Marcell Stippinger and Balázs Hangya for their time and effort to give their comments and insights about this work, which significantly improved its quality Jokes, support, meaningful discussions and chats were of utmost importance, so many thanks to Mihály Bányai, László Zalányi, Tamás Kiss, László Négyessy and Balázs Ujfalussy for being my colleagues. Furthermore I would like to express my gratitude towards my parents, who launched me on this journey and wanted my best as far as they could. During my PhD studies I had the opportunity work at the Theoretical Neuroscience and Complex Systems Research Group, Wigner Research Centre for Physics.